J Physiol 0.0 (2026) pp 1–30

The Journal of Physiology

Sedentary ageing remodels the structure–function relationships that underlie calcium signalling at super-resolution scales in the heart

Miriam E. Hurley, David Conesa, Alan P. Benson and Michael A. Colman

Department of Biomedical Sciences, Faculty of Biological Sciences, University of Leeds, Leeds, UK

Handling Editors: Eleonora Grandi & Manuel Navedo

The peer review history is available in the Supporting Information section of this article (https://doi.org/10.1113/JP290679#support-information-section).

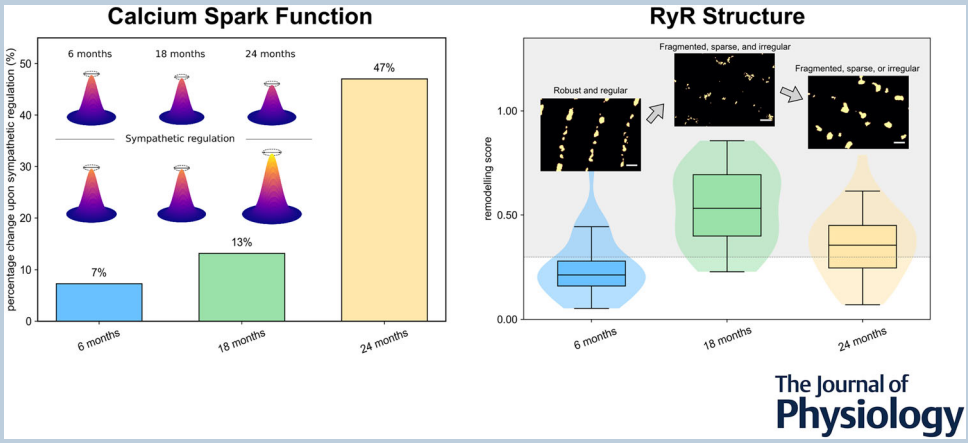

Abstract figure legend Illustration of calcium spark function and ryanodine receptor (RyR) structure within a sedentary model of ageing. Upon sympathetic stimulation from 1 μM isoprenaline a linear response to calcium spark morphology occurred, accompanied by a biphasic progression of RyR remodelling across age.

Abstract Intracellular calcium handling underpins excitation–contraction coupling in the heart, and its dysfunction has been linked to both mechanical and electrical impairments. Age-related remodelling of the structure–function relationships that underpin calcium spark morphology and dynamics may therefore be causatively linked to associated cardiac dysfunction. We aim to uncover age-dependent features of calcium spark morphology and the distribution of type-2 ryanodine receptor (RyR) clusters, responsible for intracellular calcium release. Isolated ventricular cardiomyocytes were obtained from male Wistar rats at 6, 18 and 24 months of age. Subcellular structure was assessed using expansion microscopy to localize RyR, and calcium sparks were recorded in the absence and presence of 1 μM isoprenaline using spinning disk confocal micro-

Miriam E. Hurley is a postdoctoral fellow in cardiac electrophysiology and experimental lead in the Systems Physiology Lab at The University of Leeds. Her focus is on developing and applying multiscale imaging modalities to study the functional and structural properties of the heart in a correlative manner. This focus has been applied to the investigation of cardiac remodelling in heart failure, the study of Purkinje fibres in mechanically induced arrhythmias and understanding the ageing heart.

DOI: 10.1113/JP290679

scopy. Super-resolution imaging revealed that both aged points were associated with a greater degree of cluster fragmentation, sparseness and structural disorder than the 6-month group, leading to an increased prevalence of remodelled phenotype cells in the aged groups. The 18-month group exhibited the most substantial remodelling of many properties, including the prevalence of remodelled cells, indicating either a genuine biphasic progression of remodelling with age or the divergence of structurally healthy and structurally remodelled groups with age. Moreover, ageing enhanced the impact of β-adrenergic stimulation on calcium spark morphology, increasing spark amplitude, full-width half maximum and spark mass. Our study reveals that RyR cluster properties are non-linearly remodelled with age, with RyR phosphorylation leading to remodelling of calcium spark morphology with age, which may contribute to reduced contractile performance and increased arrhythmia incidence.

(Received 1 December 2025; accepted after revision 22 June 2026; first published online 3 August 2026)
Corresponding author M. A. Colman: Department of Biomedical Sciences, Faculty of Biological Sciences, University of Leeds, Leeds LS2 9JT, UK. Email: m.a.colman@leeds.ac.uk

Key points

- Calcium spark morphology and ryanodine receptor cluster properties were assessed in a rat model of sedentary ageing at three age points.
- Calcium spark morphology was much more strongly influenced by β-adrenergic stimulation in the aged cohorts compared to the young group, corresponding to an increase in the spatial extent and overall spark mass and indicating an increased responsiveness to sympathetic regulation in ageing.
- Ageing was associated with a non-linear remodelling of the ryanodine receptor cluster pattern. At the submicron scale ageing led to an increase in fragmented-like clusters; at the broader scale ageing led to an increase in axial spacing and sparseness, as well as a reduction in the regularity of cluster distribution.
- Across all metrics the younger of the two aged groups exhibited the most substantial and highest probability of remodelling, indicating a potential biphasic progression of structure–function relationships with age, corresponding to remodelling and partial recovery.

Introduction

The healthcare challenges posed by ageing populations worldwide are a major concern of the 21st century (Lim et al., 2017). Ageing is associated with increased prevalence of cancers, neurological disorders and cardiovascular dysfunction, imposing substantial social and economic costs on individuals and societies (Fogg et al., 2024; Kallestrup-Lamb et al., 2024; Watkins & Overton, 2025). Age-related dysfunction of the heart, specifically, has been implicated as a key causative factor limiting quality of life and increasing the risk of sudden death (Costantino et al., 2016; Dai et al., 2012; Hatch et al., 2011; Lu et al., 2017; Meschiari et al., 2017; Nakou et al., 2016). Cardiovascular disease is two orders of magnitude more prevalent in those aged over 75 than in those under 45 (Bhatnagar et al., 2015) and is the leading cause of death in individuals aged over 65 (Dai et al., 2012). Physical activity is protective against the development of cardiac dysfunction (Tian & Meng, 2019); thus the burden of age-related cardiovascular disease may be exacerbated in societies characterized by sedentary lifestyles (Hajduk & Chaudhry, 2016). A deeper understanding of how the heart remodels during normal sedentary ageing may therefore provide insights essential for the development of improved diagnostic and therapeutic strategies to prevent and manage age-related cardiac dysfunction.

Cardiac ageing (Hatch et al., 2011; Nakou et al., 2016) is associated with mechanical and electrical impairment, leading to reduced pumping efficiency and increased arrhythmia susceptibility, respectively. For example, the incidence of ventricular ectopic excitation, which can act as a trigger for fatal arrhythmia events, is 17-fold higher in men aged over 60 than in those aged 20–40 (Nakou et al., 2016). Structural and functional remodelling at the cellular and tissue levels combines to produce mechanical impairment and elevated arrhythmia incidence observed with ageing.

Excitation–contraction (EC) coupling in the heart relies on calcium-induced-calcium-release (CICR), whereby L-type calcium channels (LTCCs) open during the action potential, mediating an inward current (the L-type calcium current, I_{CaL}) that activates ryanodine receptor type-2 (RyRs) channels on the sarcoplasmic reticulum (SR) membrane. This produces a much larger calcium release (a calcium spark) from this intracellular calcium store that drives cellular contraction. During relaxation various calcium effluxes ensure maintained homoeostasis, including the SR calcium pump (SERCA) that restores the SR calcium load and the electrogenic sodium–calcium exchanger (NCX) that balances the calcium influx associated with the LTCCs. The transverse and axial tubule system (t-system) ensures the delivery of the action potential into the cell interior, and LTCCs and RyRs are co-located in junctional complexes throughout the cell volume to ensure tight coupling and robust CICR in healthy myocytes. The whole-cell average intracellular calcium transient comprises the sum of thousands of spatially distributed calcium sparks that occur in discretely separated clusters of RyRs. Spatial properties of intracellular calcium handling are therefore central to both the efficiency of cellular contraction and the emergence of electrical dysfunction and provide a promising system in which to study the multiscale mechanisms of cardiovascular dysfunction.

Despite being spatially localized events, isolated calcium sparks may induce further sparks in neighbouring RyR clusters. Intracellular calcium diffusion is highly buffered, and therefore the local cytosolic calcium elevation at a neighbouring cluster that is responsible for inducing a spark depends steeply on intercluster distance. Spatial propagation of calcium sparks through this 'fire-diffuse-fire' mechanism can be adaptive, for example in enabling centripetal calcium propagation in detubulated cells (Brette et al., 2004; Greiser et al., 2014; Louch et al., 2004), or maladaptive, promoting spontaneous whole-cell calcium release and arrhythmogenic intracellular calcium waves (Aistrup et al., 2017; Cheng et al., 1996; Colman, 2019; Kazakova et al., 2025; Shah et al., 2019). Thus RyR cluster structure, spatial distribution and nearest-neighbour relationships critically determine CICR dynamics, and remodelling of t-system structure and RyR cluster properties has been causatively and mechanistically linked to dysfunction in multiple cardiac conditions, including forms of heart failure (Louch et al., 2004, 2013; Sheard et al., 2019).

We therefore aimed to determine whether calcium sparks in response to β-adrenergic stimulation and RyR cluster properties are remodelled in a sedentary ageing model. We focused our analyses on calcium spark regulation by β-adrenergic stimulation, RyR cluster size and extent and nearest-neighbour relationships at the cellular, animal and age-group levels across three age points. We report remodelling of multiple features of calcium sparks upon β-adrenergic stimulation, cluster structure and cluster distribution that often follow a biphasic progression with age, with remodelling of some features being most severe at the middle age point, whereas others remained substantially remodelled at the oldest age point. Primarily the effect of β-adrenergic stimulation on calcium spark morphology was enhanced with age, concomitant with an increase in RyR cluster fragmentation at the submicron scale and lower degree of regularity at larger scales.

Methods

Model of ageing and tissue preparation

Male adult (454–920 g) Wistar rats were obtained from Central Biomedical Services, University of Leeds, and housed according to the Guide for the Care and Use of Laboratory Animals. Animals were bred and aged in house at 20°C–22°C with 50% relative humidity on a 12 h light/dark cycle. Animals had no additional intervention, with *ab libitum* access to regular chow and water. At the required age (6, 18 or 24 months) animals were killed by rising carbon dioxide, with death confirmed by cervical dislocation, in accordance with local and national ethical regulations and approvals according to the UK Animals (Scientific Procedures) Act of 1986. Animals were randomly assigned to each of these groups at the start of the ageing process. In some cases husbandry concerns unrelated to ageing, such as long nails, limited the ability to further age individual animals assigned to the 24-month group, leading to the necessity of assigning them to the 18-month group at the time of culling.

The whole heart was quickly excised and perfused with ice-cold cardioplegic solution (mM); glucose 277.5, KCl 30, $NaHCO_3$ 25, mannitol 34.3 and 5 U/mL heparin (pH 7.4; Sigma-Aldrich, Gillingham, UK). The body, liver, lungs and heart were weighed, with the organs comparatively assessed in accordance to body weight to observe sedentary body composition in relation to age.

Ventricular cardiomyocytes were enzymatically isolated. The heart was cannulated to a Langendorff apparatus at the aorta and retrogradely perfused at 7 mL/min with oxygenated isolation solution (mM); NaCl 130, $MgCl_2$ 1.4, KCl 5.4, NaH_2PO_4 0.4, HEPES 5, glucose 10, taurine 20, creatine 10 (pH 7.4; 37°C; Sigma-Aldrich, Gillingham, UK) with added 0.75 mM $CaCl_2$. Once the circulation had cleared, isolation solution with added 0.1 mM EGTA was perfused for 4 min, followed by perfusion of isolation solution with 1 mg/mL collagenase type II (Worthington Biochemicals, USA) and 1.8 mg/mL protease (Sigma-Aldrich, Gillingham, UK) for 7 min. The ventricles were blunt dissected from the remaining tissue, triturated in enzyme solution and filtered. Iso-

lated ventricular cardiomyocytes were re-suspended in preoxygenated Tyrode's solution (mM); NaCl 140, $MgCl_2$ 4, KCl 1, HEPES 10, glucose 10, $CaCl_2$ 1.8 (pH 7.4; 20°C–22°C; Sigma-Aldrich, Gillingham, UK). Cell yield decreased linearly with age. Before experiments, cell suspensions were washed multiple times in Tyrode's solution to remove overly digested cardiomyocytes and any debris. Across all experiments ventricular cardiomyocytes that had a robust rod-like shape with clear striations visible were selected.

Assessment of calcium sparks

Confocal imaging. Isolated ventricular cardiomyocytes were loaded with 5 μM Fluo-4AM (ThermoFisher Scientific, Loughborough, UK) for 15 min at 20°C–22°C. Cells were then resuspended in Tyrode's solution for 30 min at 4°C to enable de-esterification and plated on a #1.5 glass coverslip chamber. Spontaneous calcium spark activity was recorded using a Nikon Diaphot Eclipse TE2000 inverted microscope with Nikon 60× water-immersed 1.4 NA objective attached to an Andor Revolution unit (Belfast, UK) confocal system with a Yokogawa CSU X1 spinning disk (10,000 rpm), as described by Steele & Steele (2014). Fluo-4 was excited with a 488 nm laser, and >500 nm emitted fluorescence was detected with an iXon3 897 electron-multiplying CCD camera at a range of 9.90–32.95 frames per second and at 512×512 pixel resolution. The same cardiomyocytes were then exposed to 1 μM isoprenaline (ISO), and measurements of spontaneous calcium spark acquisition were repeated.

Processing and analysis. Calcium acquisition series were loaded into FIJI *ImageJ*, and calcium sparks were detected using the xyspark plug-in (Steele & Steele, 2014). Calcium spark localization and morphology, including full width at half maximum (FWHM in μm), amplitude (F/F_0) and spark mass (AU), were estimated based on the fit of fluorescence signal to a Gaussian curve in relation to baseline fluorescence over time. Spark mass was defined as $FWHM^3$ × amplitude. Application of a 15 pixel sliding paraboloid was used to subtract background fluorescence. Calcium sparks were filtered using the following parameters: 1.0 μm ≤ FWHM ≤ 6.0 μm, 0 ≤ R^2 ≤ 0.5 and 0 AU ≤ spark mass ≤ 50 AU to ensure that only in-plane calcium sparks were analysed (Hurley et al., 2021).

Assessment of RyR cluster structure and arrangement

Super-resolution expansion microscopy. Isolated ventricular cardiomyocytes were incubated for 2 h at 37°C upon a precoated 11.9 μg/mL laminin #1.5 coverslip. Cells underwent fixation by 2% paraformaldehyde (Sigma-Aldrich, Gillingham, UK; w/v in phosphate-buffered saline; PBS) for 10 min at 20°C–22°C, followed by multiple PBS washes over 60 min. To immunolabel for RyR at 20°C–22°C cells were permeabilized for 10 min with 0.1% Triton X-100 in PBS, followed by 60 min blocking with 10% normal goat serum in PBS. Cells were incubated overnight at 4°C with RyR antibody (MA3-916; ThermoFisher Scientific, Loughborough, UK) 1:200 dilution in PBS-based incubation solution (w/v or v/v): NaN_3 0.05%, bovine serum albumin 2%, Triton X-100 0.05%. After being washed with PBS thrice, cells were incubated at 20°C–22°C for 2 h with a 1:200 dilution of Alexa 488 anti-mouse secondary antibody (A11001; ThermoFisher Scientific, Loughborough, UK) in incubation solution, before being washed with PBS thrice.

Samples underwent 4× enhanced expansion microscopy (EExM). As previously denoted by Sheard et al. (2019) 'enhanced' refers to the application of an Airyscan detector during the image acquisition process. This deconvolution step enables an in-plane resolution of 170 nm compared to standard 250 nm of confocal microscopy (Huff, 2015).

Following a previously published protocol (Sheard & Jayasinghe, 2021; Sheard et al., 2019; Tillberg et al., 2016) cells were incubated overnight at 4°C with acryloyl-X (ThermoFisher Scientific, Loughborough, UK) in PBS as an anchoring component. After being washed with PBS thrice, cells were embedded within a PBS-based monomer solution containing (w/v, Sigma-Aldrich, Gillingham, UK) sodium acrylate 8.6%, acrylamide 2.5%, *N*,*N*-methylenebisacrylamide 0.15%, NaCl 11.7%, ammonium persulfate 0.1% and *N*,*N*,*N*,*N*-tetramethylethylenediamine 0.1% for 2 h at 37°C to form a gel. These polymerized cell-containing gels were then incubated overnight at 20°C–22°C with 0.2 mg mL^{-1} proteinase K (New England Biolabs, Hitchin, UK) containing dH_2O-based digestion buffer; Tris 50 mM at pH 8.0 (ThermoFisher Scientific, Loughborough, UK), ethylenediaminetetraacetic acid 1 mM (Sigma-Aldrich, Gillingham, UK), Triton X-100 0.5% and guanidine HCl 0.8 M (Sigma-Aldrich, Gillingham, UK). The next day digestion buffer was removed, and dH_2O washes repeated every hour to expand the gel until a size plateau was reached. Before imaging, the macroscale expansion factor was obtained by measuring the postexpansion gel size. Expansion factor was calculated by comparing postexpansion gel size to preexpansion size after gel polymerization. Resultingly within our 4× EExM experiments we had the ability to achieve an in-plane resolution < 40 nm and an axial resolution < 90 nm (Sheard et al., 2022).

Postexpanded gels were imaged at 20°C–22°C on #1.5 coverslips in custom-made acrylic chambers. Imaging was undertaken upon an LSM880 inverted microscope (Carl

Zeiss, Jena, Germany) using a 40× oil immersion 1.4 NA objective and Airyscan detector. A 488 nm DPSS laser excitation was selected, with emission bands selected by the in-built detector. Images were acquired using *ZEN* software, with Airyscan deconvolution applied.

Image processing: RyR cluster properties. Acquired images underwent a background subtraction within FIJI *ImageJ* using a 50-pixel radius sliding paraboloid function. Analysis of RyR cluster properties was performed using custom-built Python code, which we provide in the associated Zenodo repository. The monochromatic image file was thresholded to remove low-intensity noise (0.125–0.3 × maximum intensity) and a binary mask created (Fig. 1*Aa,b*). Individual clusters in the binary mask were identified, and the pixel area for each cluster was calculated. This pixel area was converted to estimate the number of RyRs (N_{RyR}) given the image resolution (40–170 nm) and expansion ratio (3.8) and assuming for the purpose of this analysis that a single channel occupies 29 × 29 nm^2 (Baddeley et al., 2009). Clusters containing fewer than three RyRs (corresponding to 2–20 pixels across the whole dataset) were excluded, and all subsequent analyses were performed on clusters of three or more RyRs.

A co-ordinate frame that was orientated to the myocyte was defined, with the *x*-axis aligned to the axial direction and the *y*-axis to the transverse direction (Fig. 1*Ac*). This rotated co-ordinate frame forms the basis for calculating cluster extents and the derived inter-neighbour distances. Note that the image itself was not rotated. Alignment of the rotated co-ordinate frame can be verified by the emergence of the multimodal x-positions histogram if the underlying data contain a sufficiently regular, repeating pattern of transverse cluster lines. Cluster height (extent in the transverse, *y*, direction) and width (extent in the axial, *x*, direction) were calculated directly (Fig. 1*Ad*). The co-ordinate frame rotation was performed on an image-by-image basis, and the transverse orientation of cluster patterns did not necessarily remain exactly parallel across the field of view; the best-fit rotation was selected based on visual judgement.

Image processing: cluster arrangement and neighbour relationships. First the 12 nearest neighbours for each cluster were found based on the centre-to-centre distances (Fig. 1*Ba*). Based on the angles between the line defining the neighbour connection and the axial direction of the cell, the connection was categorized as being either primarily transverse or axial, enabling each neighbour type to be considered independently. This defines the 'full' neighbour map. A second neighbour map was created that identified only the closest neighbour to each cluster in the four principal directions ($\pm x$ and $\pm y$). This 'directional' neighbour map (Fig. 1*Bb*) forms the basis for most analyses concerning inter-neighbour relationships performed in this study. Note that despite this map imposing that only the closest neighbour in each of the four directions is retained, a single cluster can still have more than four neighbours if it itself is the first closest neighbour in any given direction to multiple other clusters, for example where one cluster is axially adjacent to a cluster of clusters at the next transverse line.

Edge-to-edge distances were then calculated (Fig. 1*Bc*). Where there was orthogonal overlap between clusters, the edge-to-edge distance corresponded to the transverse distance between the upper extent of a given cluster and the lower extent of its neighbour in the positive *y* direction, or the axial distance between the rightmost extent of the first cluster and the leftmost extent of its neighbour in the positive *x* direction. Where there was no overlap the edge-to-edge distance was calculated as the distance between the closest corners of the bounding boxes of the two clusters, i.e., the minimum distance between them. Edge-to-edge distances were calculated only for the corresponding neighbour type (i.e. transverse edge-to-edge distance was not computed for axial neighbours and vice versa).

Analysis of the statistics and distributions was performed on the directional neighbour map on a cluster-by-cluster basis (i.e. considering the population of clusters that contained centre-to-centre or edge-to-edge distances at each given bin). This means that many neighbour connections are double counted (appearing for both clusters to which it connects), which is suitable for cluster-wise analysis but not for assessing the proportion of neighbour connections that fulfil a given criterion. For this neighbour-wise analysis a unique neighbour map was created from the full or directional neighbour maps that accounts for each connection only once.

Image processing: categorizing structural phenotypes. To evaluate the above measures of RyR heterogeneity in aggregate and identify different structural features we developed a suite of structural metrics to categorize individual cells. First we explored RyR cluster fragmentation. However we are careful not to imply a fragmentation process that we have not directly observed and therefore introduce the terminology 'cluster ensembles' to refer to regions where multiple small clusters are found in close proximity, which may typically be referred to as 'fragmented'.

Analysis of cluster ensembles was first performed by counting, for each image, the number of neighbouring clusters that were within a threshold (0.1–1.1 μm) for the edge-to-edge distances, and calculating the proportion of clusters that contained two or more, three or more, or four or more neighbouring clusters within this threshold.

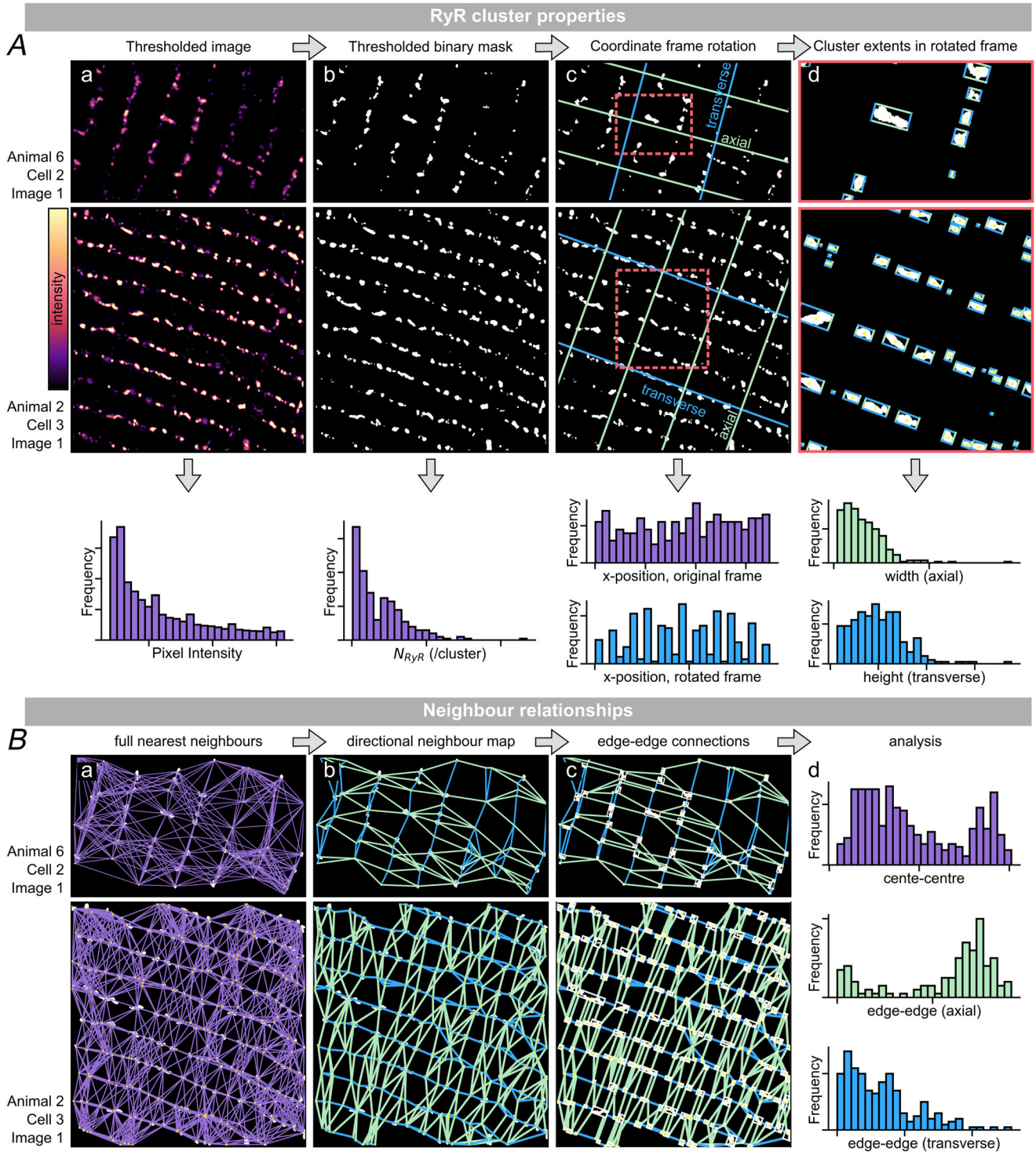

Figure 1. Ryanodine receptor (RyR) cluster image processing pipeline
A, processing of images to determine RyR cluster properties. Two examples where the field of view and orientation of the images are very different are shown for illustration of the general applicability of the approach. The pipeline illustrating image thresholding *(a)*, the application and cleaning of a binary mask *(b)*, the overlay of a rotated co-ordinate frame *(c)* and the identification of cluster extents in the rotated frame *(d)*. Histograms are provided for illustrative purposes only. *B*, processing of neighbour relationships. On the same two original images illustrated are the nearest neighbour maps *(a)*, directional neighbour maps highlighting the transverse (blue) and axial (green) connections *(b)*, edge-to-edge connections (and bounding boxes) *(c)* and the neighbour distance data that can be obtained from the method *(d)*.

This metric, however, failed to identify regions of cluster ensembles in cells that were generally robust elsewhere. We therefore further explored relationships on a granular neighbour-by-neighbour basis. For each neighbour connection (from the unique directional neighbour map) the edge-to-edge distances were correlated with the average N_{RyR} of the two clusters associated with the connection. It was empirically decided that a suitable metric for the prevalence of cluster ensembles was to count the proportion of neighbour connections that fit below a contour in the phase space of average N_{RyR} *vs.* edge distance (Fig. 2*B*):

$$\text{Cluster ensemble score} = \frac{1}{N_{\text{connections}}} \sum_{i=1}^{N} \left[\left(\frac{\left(N_{\text{RyR},1} + N_{\text{RyR},2}\right)/2}{35} \right)^2 + \left(\frac{\text{edge distance}}{0.8} \right)^2 \leq 1 \right]$$

where the factor 35 is the maximum average N_{RyR} of adjacent clusters for them to be considered part of an ensemble, and 0.8 μm is the maximum edge-to-edge separation. The contour imposes that larger clusters must be closer together to be considered part of an ensemble, whereas small clusters may approach that upper distance limit and still be counted. It was determined that a cluster ensemble score of above 0.2 (i.e. where 20% of the neighbour connections are associated with cluster ensembles) would lead to a cell being considered to have a high prevalence of cluster ensembles.

Measures of structure on a larger scale were assessed on a coarse-grained cluster and neighbour map (Fig. 2*C*). Coarse graining was achieved by merging adjacent clusters that fit within a given distance (0.3 μm) and size ($N_{RyR} < 50$). The same tools to process the neighbour maps were then applied to the coarse-grained data. This removes small-scale features, enabling characterization of the sparseness and regularity of structure on this larger scale.

Multiple metrics were considered to characterize sparseness and structural regularity. Relatively crude approaches were finally selected as these offered the cleanest, simplest and most accurate characterizations that could be found for our data. We note, however, that we are not intending to present these as a generally robust set of tests for all future data, but, rather, found them useful for quantification of subjective considerations in our data.

Regularity (Fig. 2*C*) was quantified by determining the proportion of edge-to-edge connections in each direction that had zero angle relative to that direction (i.e. the connection is aligned along the axes), which is a measure of the proportion of adjacent clusters whose extents overlap in the relevant orthogonal direction. A cell was determined to have irregular transverse structure if this metric was below 0.6 and irregular axial structure if this metric was below 0.4.

Sparseness (Fig. 2*D*) in the transverse direction was measured by calculating the proportion of transverse edge-to-edge distances of the directional, coarse-grained neighbour map that were greater than 0.75 μm; a cell was determined to be sparse in the transverse direction if this metric was above 0.3 (i.e. 30% or more of the transverse closest-neighbour distances in the coarse-grained model were greater than 0.75 μm). Axial spacing was defined by the mode of the *x*-component of the centre-to-centre axial distances. Overall sparseness was defined by the product of the transverse sparseness and the axial spacing, and a cell was considered sparse if this metric was greater than 0.75.

Despite the crudeness of these metrics they were able to accurately identify and score images that correlated with visual agreement about the structure (Fig. 2). The thresholds also enable the calculation of the proportion of animals that contained a high degree of each measure, which we refer to as the probability of each metric for each age group. Probability was determined by calculating the proportion of RyR datasets per animal that reached the denoted thresholds and dividing the sum by the number of animals per age group. This provides a clear indication of the average tendency of each age group on an animal-by-animal basis.

Statistical analyses

Data were tested for normality of distribution using the Shapiro–Wilk test. Body composition data (parametric) were analysed using a one-way independent ANOVA. Calcium spark data were assessed for each age group with a paired Student's *t* test. RyR data were assessed using a linear mixed model with a hierarchical structure where individual cell measurements were clustered within animals and the factor was age. Pairwise comparisons were made using Bonferroni *post hoc* tests. Where observed distributions were bimodal, Hartigan's dip test of unimodality (Hartigan & Hartigan, 1985) was used to test this. Significance (α) level was set at 0.05. RyR cluster properties and calcium spark data were collated by averaging the population density distributions for visualization, over which the hierarchical stats were overlain.

Results

Evaluation of sedentary ageing model

Body composition changed with age (Table 1). Notably body weight increased steadily over time, with a 26.6%

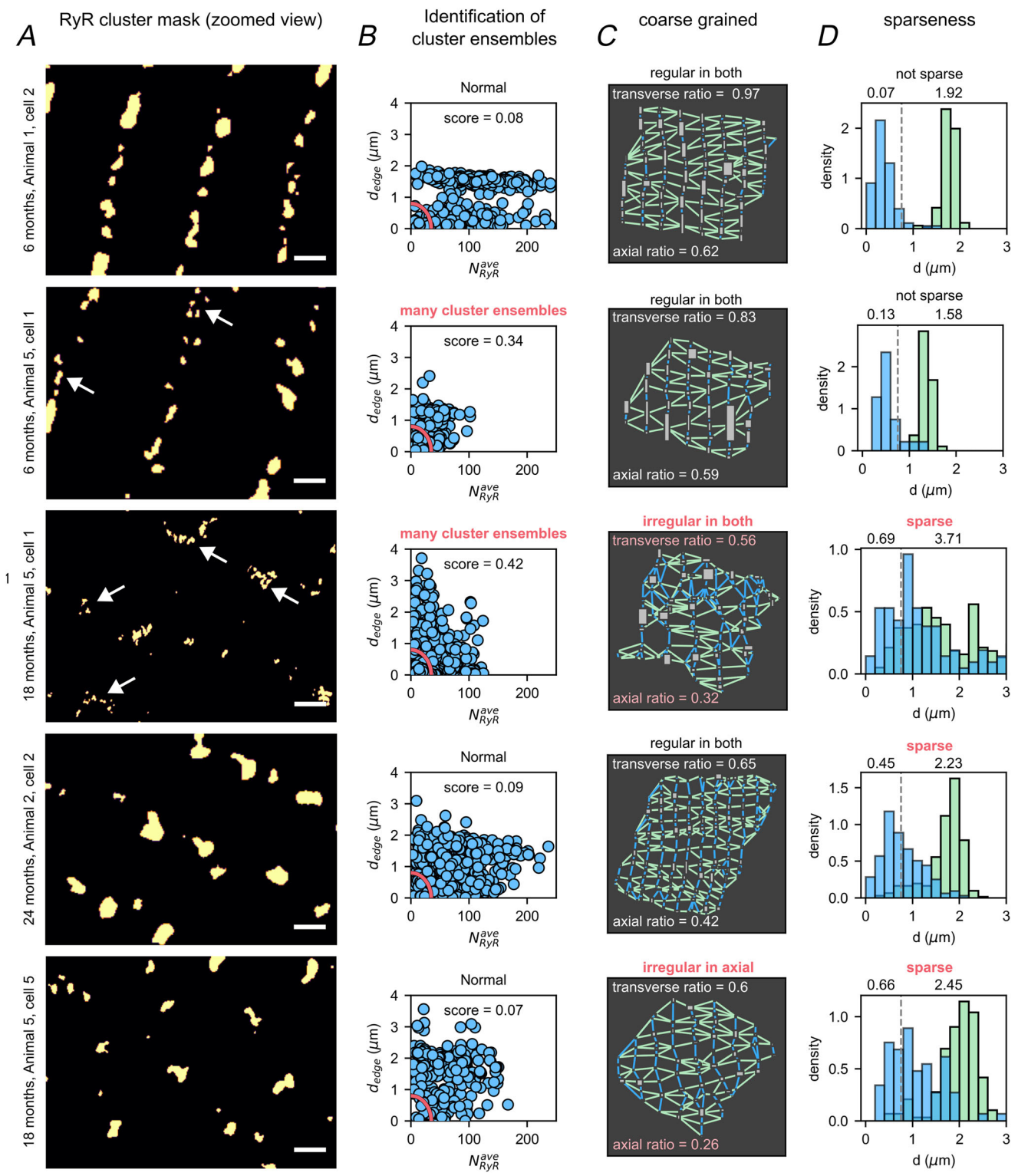

Figure 2. Illustration of structural phenotype metrics
A, zoomed view of the binary mask illustrating local ryanodine receptor (RyR) cluster structure and arrangement. Scale bar is 1 μm. *B*, the cluster ensemble score is based on the correlation between the average N_{RyR} of a neighbouring cluster pair and its edge-to-edge distance. The proportion of neighbour pairs lying within the contour illustrated by the red arc determines the score. *C*, illustration of the coarse-grained model and edge-to-edge neighbour connections. The transverse and axial regularity scores are determined by the proportion of each

neighbour connection type that is aligned along the relevant axis. *D*, the sparseness scores are based on the distribution of the transverse edge distances (blue) and the axial spacing, determined from the distribution of the *x*-component of the axial centre distances (green) in the coarse-grained model. Annotated number on the top left of each panel is the transverse sparseness score, calculated as the proportion that lies above 0.75 μm (dotted line), and the other annotated number is the axial spacing, corresponding to the mode of the axial centre *x*-component distribution.

Table 1. Sedentary rodent model of age

Age	Number	Body weight (g)	Heart weight (g)	Body:liver ratio	Body:lungs ratio	Body:heart ratio
6 months	8	533 ± 39.9	3.37 ± 1.21	0.029 ± 0.003	0.004 ± 0.000	0.006 ± 0.002
18 months	6	726 ± 92.0*	3.48 ± 0.95	0.028 ± 0.002	0.003 ± 0.001*	0.005 ± 0.001
24 months	7	803 ± 98.7*	3.73 ± 0.26	0.027 ± 0.005	0.003 ± 0.001*	0.005 ± 0.001

Note: Body composition of adult male Wistar rats across three age points; 6 months ($N = 8$), 18 months ($N = 6$) and 24 months ($N = 7$). Body weight was measured in isolation, significantly increasing upon age compared to the 6-month baseline. Body weight in relation to the liver, lungs and heart, however, did not alter with age. Data are presented as mean ± SD using one-way ANOVA.
* $P < 0.05$.

increase between 6 and 18 months ($P < 10^{-5}$) and 33.6% increase between 6 and 24 months ($P < 10^{-5}$). This weight gain was attributed to fat deposits, with a decreased trend in body:liver ratio, highlighting an increased fat distribution with age. Compared to the 6-month baseline, body:lungs ratio was decreased at 18 months ($P = 0.004$) and 24 months ($P = 0.002$) of age, suggesting respiratory insufficiency to match the increased weight gain. Minimal change in the body:heart ratio indicates no change in gross heart morphology. Heart weight increased with age (Fig. A1), with a 3.2% increase between 6 and 18 months ($P > 0.99$) and a 9.7% increase between 6 and 24 months ($P > 0.99$), suggesting that neither hypertrophy nor dilatation was present to a notable degree. We therefore have confidence that we are utilizing a sedentary model of ageing within our study. In addition, for all RyR cluster pattern measurements, correlation with body weight (Fig. A2) and body-to-heart weight ratio for each animal was assessed (Fig. A3). Our results suggest that age, and not body composition, is the determining factor for the observed changes within our model.

Calcium sparks

Due to differences in calcium spark acquisition rate, comparisons across age cannot be undertaken. Instead the age dependency of regulation by β-adrenergic stimulation was evaluated by characterizing calcium spark morphology in the absence and presence of ISO within young (6 months) and aged (18 and 24 months) rats, given that these experiments were performed under the same conditions for each cell.

ISO did not lead to statistically significant changes in any of the measures of calcium spark morphology in the 6-month group ($P = 0.605$ for FWHM, $P = 0.955$ for amplitude and $P = 0.761$ for spark mass). In both aged groups ISO led to statistically significant alterations in all measurable features of calcium spark morphology (Fig. 3). In both aged groups FWHM (Fig. 3*a*) was increased under the application of ISO. This increase was most substantial in the 24-month group (+18.2%, $P < 10^{-6}$) compared to the 18-month group (+7.0%, $P = 0.031$). Amplitude (Fig. 3*b*) was decreased in the 18-month group (−2.7%; $P < 10^{-6}$) and increased in the 24-month group (+22.4%; $P < 10^{-6}$). Spark mass, a weighted integrated measure of FWHM and amplitude to which FWHM contributes the most, was increased in both age groups (+13.2%, $P = 0.001$ in the 18-month group and +47.0%, $P < 10^{-6}$ in the 24-month group).

Substantial interanimal variability was observed in all three age groups (Fig. 3 and Fig. A4). ISO further increased the variability of the amplitude in the 18-month group and the FWHM and spark mass of the 24-month group. As such we noted that within the 18-month group, sparks with a greater amplitude were highly correlated with those that had a smaller FWHM (Fig. A5), corresponding to the same spark mass contours as other lower amplitude calcium sparks. ISO also increased the spontaneous spark frequency by approximately 50% in the 24-month group but had no discernible impact on frequency in the 6- and 18-month groups. Limitations of the analysis software meant that calcium spark duration was not acquired, and therefore these data were deemed inappropriate for a more detailed quantification of spontaneous spark frequency.

Age-stratified analysis therefore revealed that in young rats (6 months) ISO did not significantly alter calcium spark morphology, but as age increased ISO had a significant impact upon calcium spark FWHM, amplitude and spark mass, with the greatest change seen at 24 months.

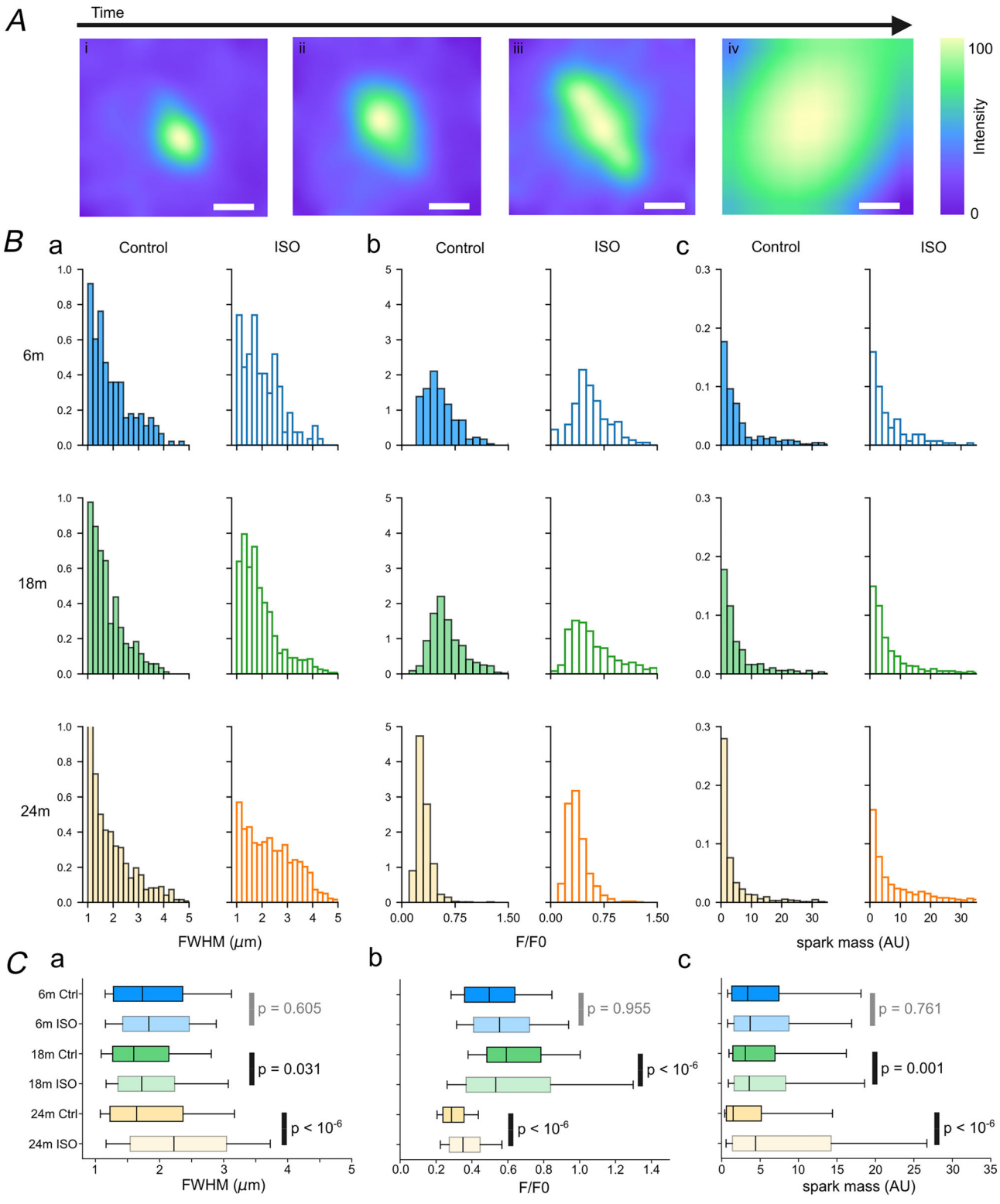

Figure 3. Spontaneous calcium spark morphology in presence of isoprenaline (ISO)
A, illustration of a spontaneous calcium spark visualized across four frames (Ai–iv), each 32.95 ms in duration. The scale bar denotes 2 μm. *B*, calcium spark properties across age at 6 months (blue; $N = 6$), 18 months (green; $N = 5$) and 24 months (orange; $N = 7$), recorded in presence of 1.8 mM calcium (solid bars) and in presence of 1 μM ISO (outline) for the full width at half maximum (FWHM) *(a)*, amplitude (F/F0) *(b)* and spark mass *(c)*. *C*, boxplots denoting median ± 5th and 95th percentiles (lower) for the FWHM *(a)*, amplitude (F/F0) *(b)* and spark mass *(c)*. Statistical overlays are based on the analysis from a paired Student's *t* test.

RyR cluster size

Across all age groups variability in RyR cluster organization was observed on an animal-to-animal basis (Figs A6 and A7). Structural heterogeneity is illustrated in the comparison of cellular regions containing the smallest RyR clusters (Fig. 4*Aa–c*) to regions containing the largest clusters (Fig. 4A*d–f*) at all age points. The extent of animal-to-animal variability was probed through analysing the absolute deviation from the median, per animal median *vs.* interquartile range and per animal mode *vs.* 95th percentile.

Median N_{RyR} per cluster (Fig. 4*B*) showed no statistically significant differences between age groups ($P > 0.99$ for 6 months *vs.* 18 months; $P = 0.3$ for 18 months *vs.* 24 months; and $P = 0.1$ for 6 months *vs.* 24

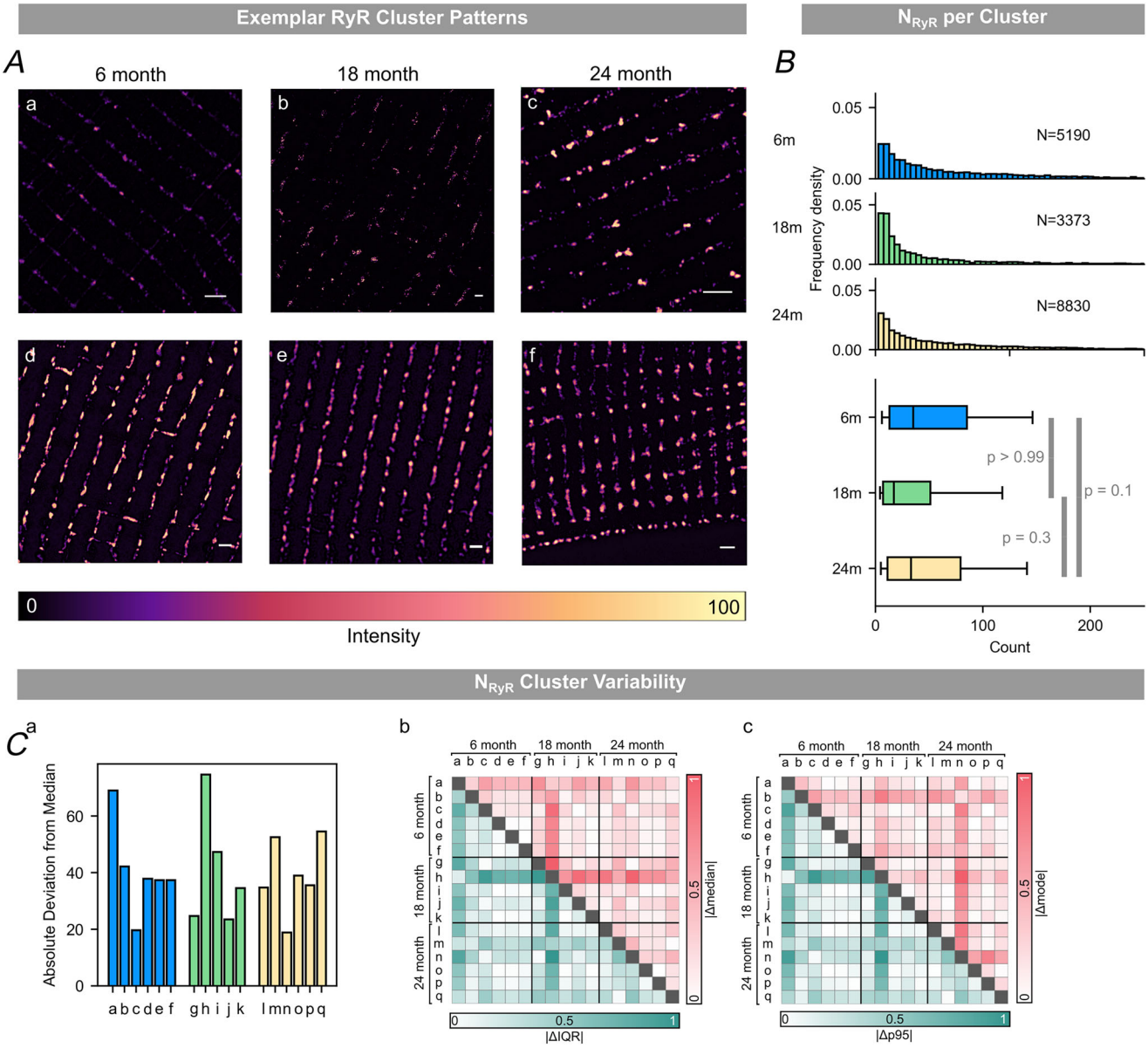

Figure 4. Ryanodine receptor type 2 (RyR) cluster pattern within ventricular cardiomyocytes across age
A, illustration of exemplary RyR cluster patterns taken from images with the smallest number of puncta per cluster (*a–c*) and largest number of puncta per cluster (*d–f*) from the 6-month (*a, d*), 18-month (*b, e*) and 24-month (*c, f*) groups. Scale bar: 1 μm. *B*, summary histograms (upper) across age at 6 months (blue; $N = 6$), 18 months (green; $N = 5$) and 24 months (orange; $N = 6$) and boxplots (lower) denoting median ± 5th and 95th percentiles (*b*), collating all data from each group. Statistical overlays are based on the analysis from the linear mixed model. *C*, interanimal variability showing the absolute deviation from the median (*a*), absolute magnitude of animal-to-animal comparisons for the median (*b*, upper right half; white-to-red), IQR (*b*, lower left half; white-to-green), mode (*c*, upper right half; white-to-red) and 95th percentile (*c*, lower left half; white-to-green).

months). Heterogeneity in RyR clustering was apparent within each age group and across young *vs.* aged. Inter-animal variability was largest in the 18-month group (Fig. 4*C*), with intercellular variability (Fig. A7) within each animal most evident within the aged rats (18- and 24-month groups).

RyR cluster neighbour relationships

Transverse neighbour relationships and correlation with cluster height. The relationships between neighbouring RyR clusters in the transverse direction exhibited significant remodelling between the young (6 months) and aged groups (18 and 24 months). Compared to the young 6-month group both aged groups observed an increase in the median centre-to-centre distances (Fig. 5*Aa*). This increase was most substantial in the 18-month group (from 0.62 to 0.68 μm; $P < 10^{-3}$) and intermediary in the 24-month group (from 0.62 to 0.67 μm; $P < 10^{-3}$). This decrease in median centre-to-centre distance from 18 to 24 months ($P < 10^{-3}$) corresponds to a biphasic age dependency, which was also observed in the variability, wherein the 18-month group exhibited the largest degree of variability, and the 24-month group exhibited intermediary variability (Fig. 5*Ba*; Figs A6*E*, A8).

Edge-to-edge distances followed a similar biphasic pattern, with the median significantly increased in both aged groups compared to the 6-month group (Fig. 5*Ab*), most substantially for the 18-month group (+26.7% compared to 6-month group; $P < 10^{-5}$) and intermediary at 24 months (+16.5% relative to 6 months, $P < 10^{-3}$), with the 24-month group having a decreased median distance relative to 18-month group (−12.2%, $P < 10^{-3}$). Variability was comparable between the 6- and 24-month groups but substantially increased in the 18-month group (Fig. A6*G*).

Cluster height (Fig. 5A*c*) was significantly reduced in both aged groups compared to the 6-month controls ($P < 10^{-6}$), most substantially at 18-month group (−48.3% change to the median), with no statistically significant differences between the two aged groups ($P = 0.5$). Interanimal variability was considerable across all measures and age groups, but most notable within the two aged groups, with individuals observed to have substantially different properties to others within and between groups (Fig. 5*B*).

Thus we observed an increase in the edge-to-edge transverse distances in age. This was a consequence of both an increase in intercluster spacing (centre-to-centre distances) and a reduction in cluster height and was most prominent in the 18-month age group.

Axial neighbour relationships and correlation with cluster width. The relationships between neighbouring RyR clusters in the axial direction also exhibited significant remodelling between the young and aged groups (Fig. 6). Centre-to-centre distances (Fig. 6*Aa*) decreased progressively with age, corresponding to a total 9% reduction at 18 months and 12% reduction at 24 months compared to the 6-month median of 1.51 μm ($P < 10^{-5}$ for all comparisons). Edge-to-edge distances (Fig. 6*Ab*) were not statistically remodelled at 18 months ($P = 0.2$ *vs.* 6 months) but were significantly reduced at 24 months (1.03 μm) compared to both 6- (1.24 μm) and 18-month (1.15 μm) groups ($P < 10^{-5}$ for both comparisons); variability was most substantial in the 18-month group (Fig. 6*B*). Cluster width (Fig. 6*Ac*) was not significantly remodelled in either age group compared to the 6-month group ($P = 0.4$ for both comparisons) but was significantly increased in the 24-month group compared to the 18-month group ($P = 0.02$).

These results indicate a consistent reduction in the axial distance between clusters that corresponds either to a decreased global axial spacing (inter-t-tubule distance) or less regular 'transverse lines'; this was further assessed during structural phenotyping at the coarse-grained level (see 'Results: categorizing structural phenotypes').

Categorizing structural phenotypes. An increase in the prevalence of 'cluster ensembles', corresponding to clusters containing multiple local neighbours, was observed for the 18-month group for distance thresholds of 0.4 μm and below, with an increase in the variability at larger distances (Fig. 7); the 24-month group was similar to the 6-month group but with a general increase in variability. This implies a larger degree of cluster ensembles in the 18-month group compared to both the 6-month controls and older, 24-month group.

This was further quantified through application of the cluster ensemble metric. A high degree of intercellular and interanimal variability was observed in the cluster ensemble score (Fig. 8*Aa*). The prevalence of cluster ensembles increased between the 6- and 18-month groups ($P = 0.065$) and was restored in the 24-month group to values similar to those of the 6-month control ($P > 0.99$). The 18-month group had the highest probability of cluster ensemble prevalent cells (46%) compared to the 6-month (35%) and 24-month (25%) groups (Fig. 8*Aa*).

Transverse sparseness (Fig. 8*Ab*) was observed to be significantly different between all three groups ($P < 10^{-3}$ for 6- *vs.* 18-month groups and 18- *vs.* 24-month groups; $P = 0.015$ for 6- *vs.* 24-month groups). The mean ± SD transverse sparseness score was largest within the 18-month group (0.53 ± 0.19), smallest within the 6-month group (0.24 ± 0.15) and intermediary within the 24-month group (mean of 0.36 ± 0.17). The 6-month group had the lowest probability of transverse sparseness (20%) compared to the 18-month (85%) and 24-month (57%) groups. Therefore transverse sparseness

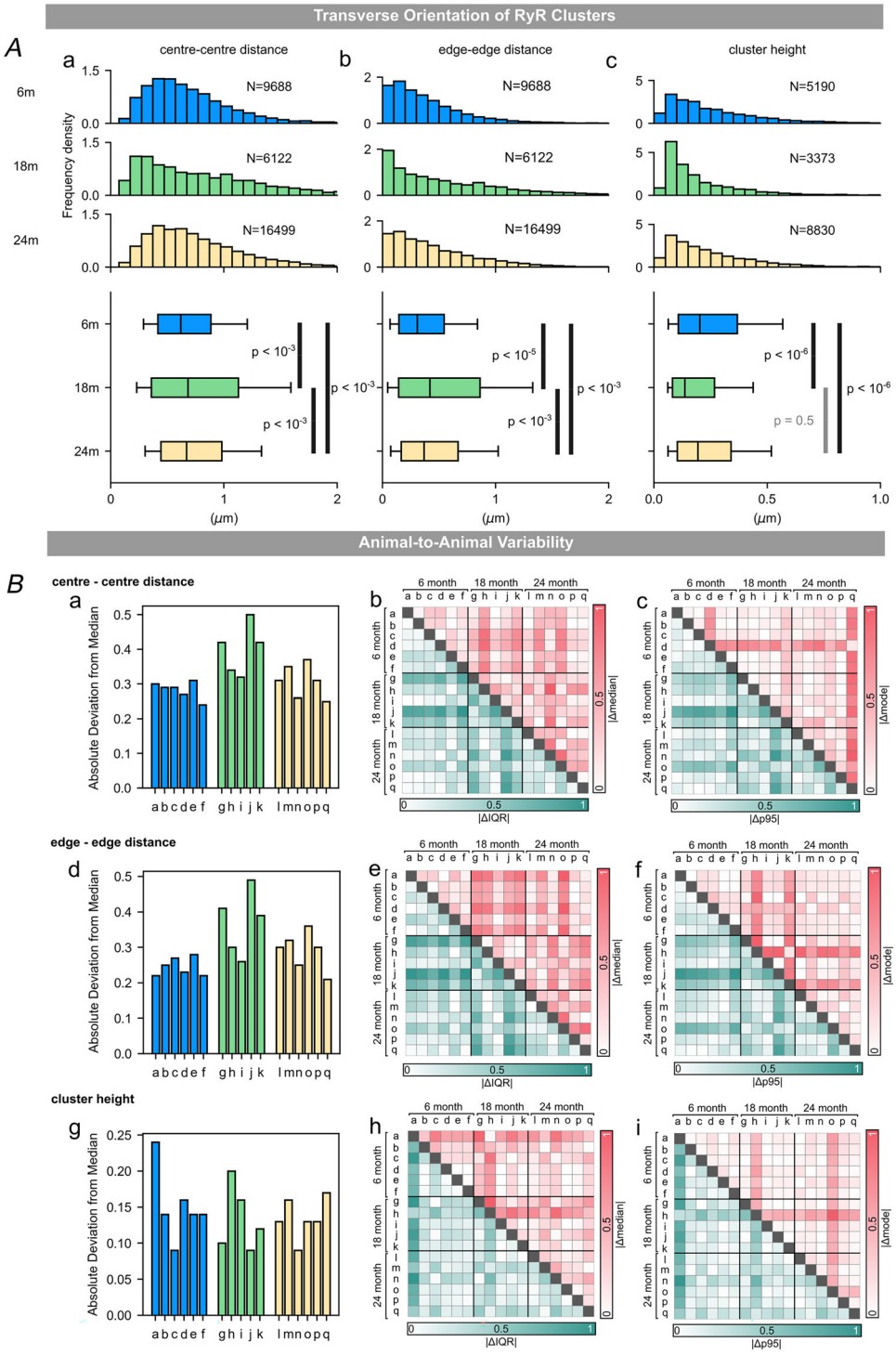

Figure 5. Ryanodine receptor transverse neighbour relationship and cluster height within ventricular cardiomyocytes across age

A, cluster properties across age at 6 months (blue; *N* = 6), 18 months (green; *N* = 5) and 24 months (orange; *N* = 6), illustrating histograms (upper) and boxplots denoting the median ± 5th and 95th percentiles (lower) for centre-to-centre transverse distance between clusters (*a*), edge-to-edge transverse distance between clusters (*b*) and cluster height *(c)*. Statistical overlays are based on the linear mixed model analysis. *B*, interanimal variability showing the absolute deviation from the median (*a, d, f*), and the absolute magnitude of animal-to-animal comparisons for the median (*b, e, h*; upper right half; white-to-red), interquartile range (IQR) (*b, e, h*; lower left half; white-to-green), mode (*c, f, i*; upper right half; white-to-red) and 95th percentile (*c, f, i*; lower left half; white-to-green).

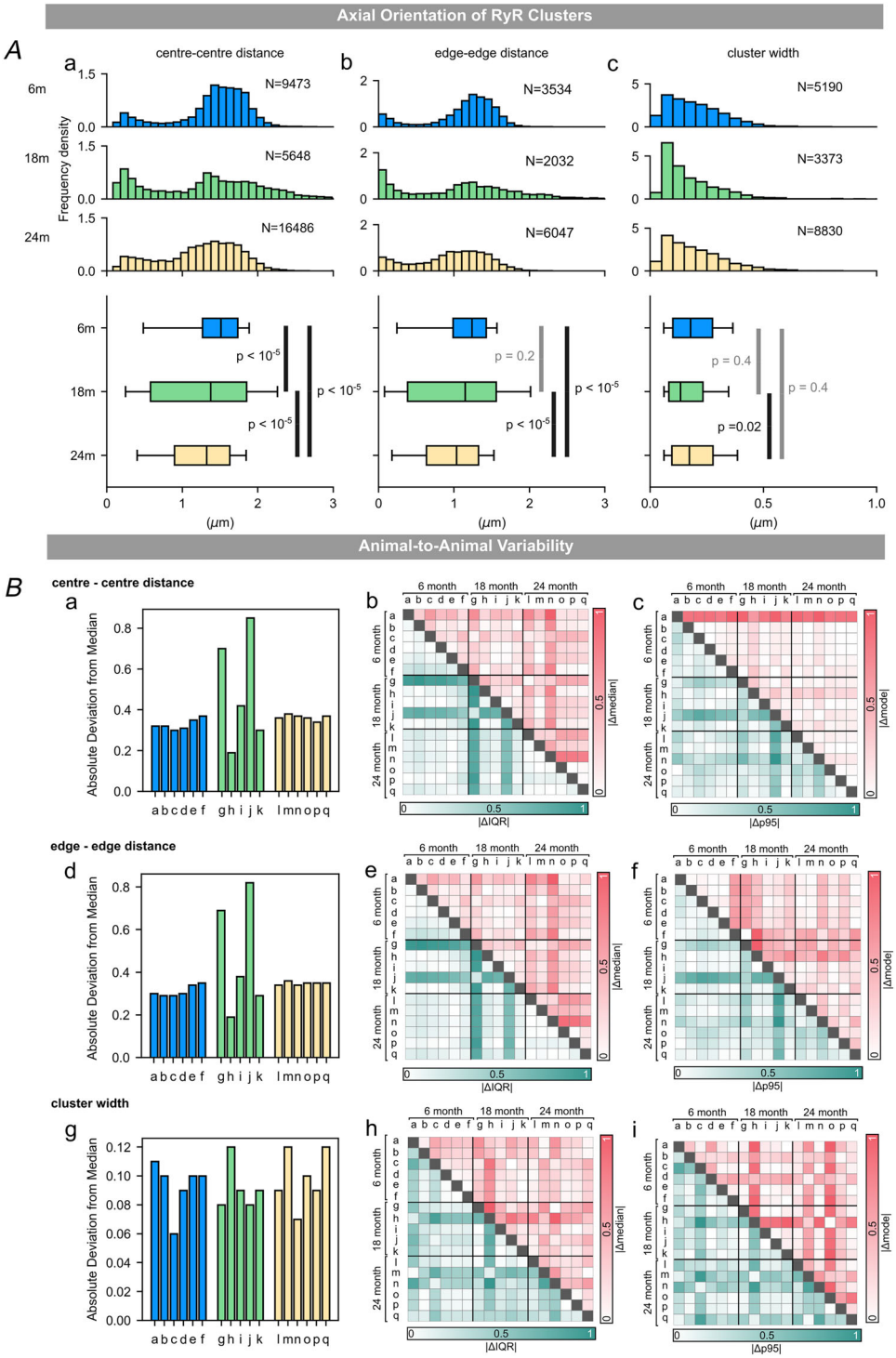

Figure 6. Ryanodine receptor axial neighbour relationship and cluster height within ventricular cardiomyocytes across age

A, cluster properties across age at 6 months (blue; $N = 6$), 18 months (green; $N = 5$) and 24 months (orange; $N = 6$), illustrating histograms (upper) and boxplots denoting the median ± 5th and 95th percentiles (lower) for centre-to-centre axial distance between clusters (*a*), edge-to-edge axial distance between clusters (*b*) and cluster width (*c*). Statistical overlays are based on the linear mixed model analysis. *B*, interanimal variability showing the absolute deviation from the median (*a, d, f*), and the absolute magnitude of animal-to-animal comparisons for the median (*b, e, h*; upper right half; white-to-red), interquartile range (IQR) (*b, e, h*; lower left half; white-to-green), mode (*c, f, i*; upper right half; white-to-red) and 95th percentile (*c, f, i*; lower left half; white-to-green).

was increased in the 18-month group and only partially recovered in the 24-month group.

Axial spacing (Fig. 8*Ac*) was observed to be significantly different between the 6- and 18-month groups ($P = 0.004$) and the 18- and 24-month groups ($P = 0.009$) but was statistically indistinguishable between the 6- and 24-month groups ($P > 0.99$). The 18-month group had the largest mean (2.12 μm *vs.* 1.7 μm in the 6- and 24-month groups), which accentuated the increased transverse sparseness and resulted in the 18-month group having the largest overall sparsity (Fig. 8*Ad*; $P < 10^{-3}$ *vs.* both other groups); only a moderate difference was observed between the 6- and 24-month groups ($P = 0.098$). Thus sparseness increased substantially from the 6- to 18-month groups and was only partially restored in the 24-month group. The overall probability of sparseness was only 8% in the 6-month group, increasing to 55% in the 18-month group and 31% in the 24-month group.

Transverse regularity (Fig. 8*Ae*) was significantly reduced in the 18-month group compared to the 6-month group ($P < 10^{-3}$) and remained reduced in the 24-month group ($P = 0.002$ *vs.* 6-month group) but was only moderately different between the 18- and 24-month groups ($P = 0.088$). The probability of finding transverse irregularity increased from 3% in the 6-month group to 29% at the 18-month and 25% at 24-month groups.

Axial regularity (Fig. 8*Af*) was significantly different between the 18-month group and both other groups ($P < 10^{-3}$) but was not significantly different between the 6- and 24-month groups ($P = 0.574$), corresponding to a reduction in the mean regularity from 0.55 at 6-month group to 0.39 at 18-month group, which was restored to 0.51 at 24-month group. The SD was largest for the 24-month group (1.29 *vs.* 1.07 for the 6-month and 18-month groups), which was reflected in an overall increase in the probability of finding axial irregularity at

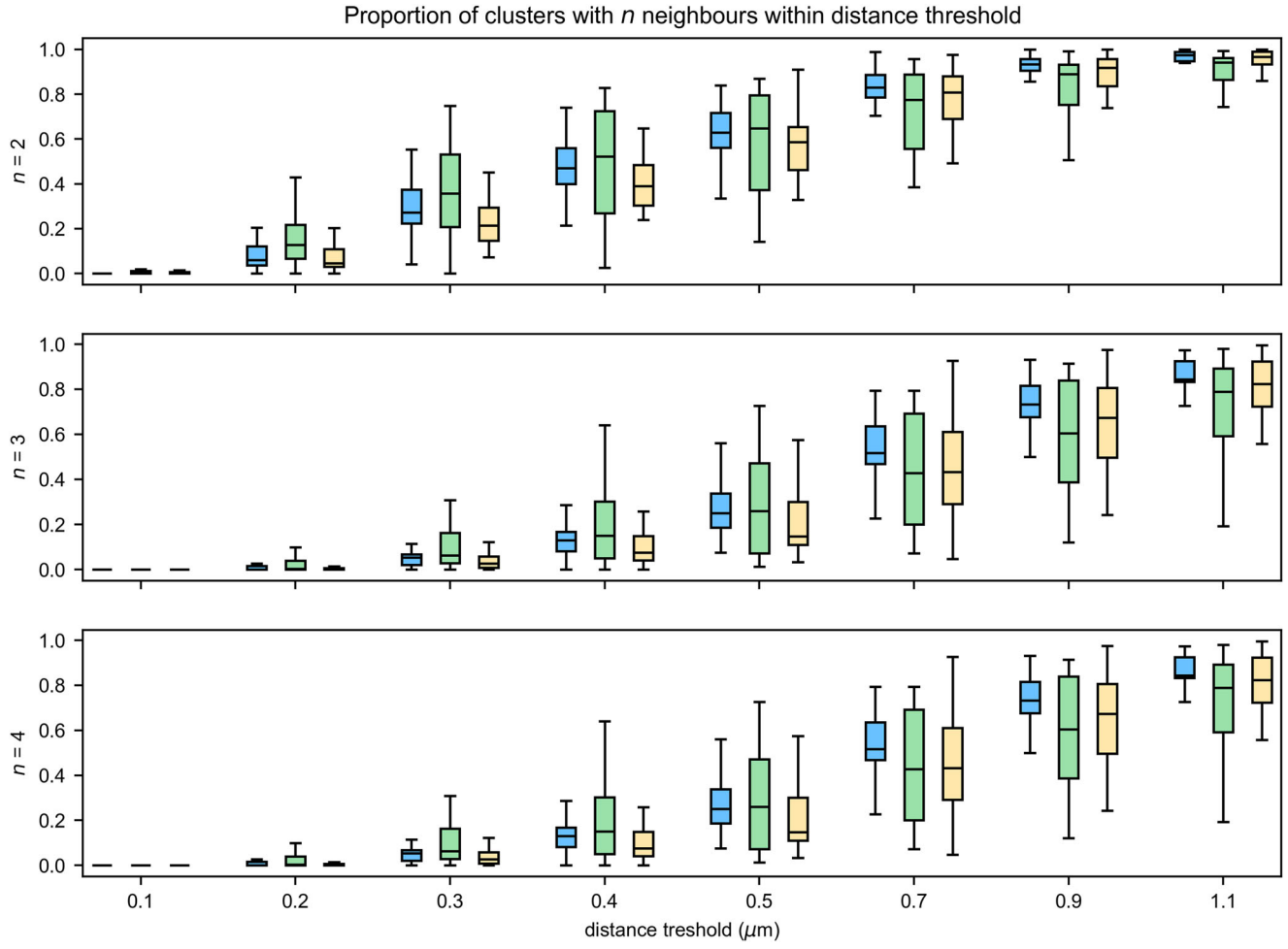

Figure 7. Analysis of clusters-of-clusters
For all three age groups (blue – 6 months; green – 18 months; orange – 24 months) the distributions describing the proportion of clusters that contained two (upper), three (middle) or four (lower) neighbouring clusters within varying distance thresholds are shown as boxplots denoting median ± 10th and 90th percentiles.

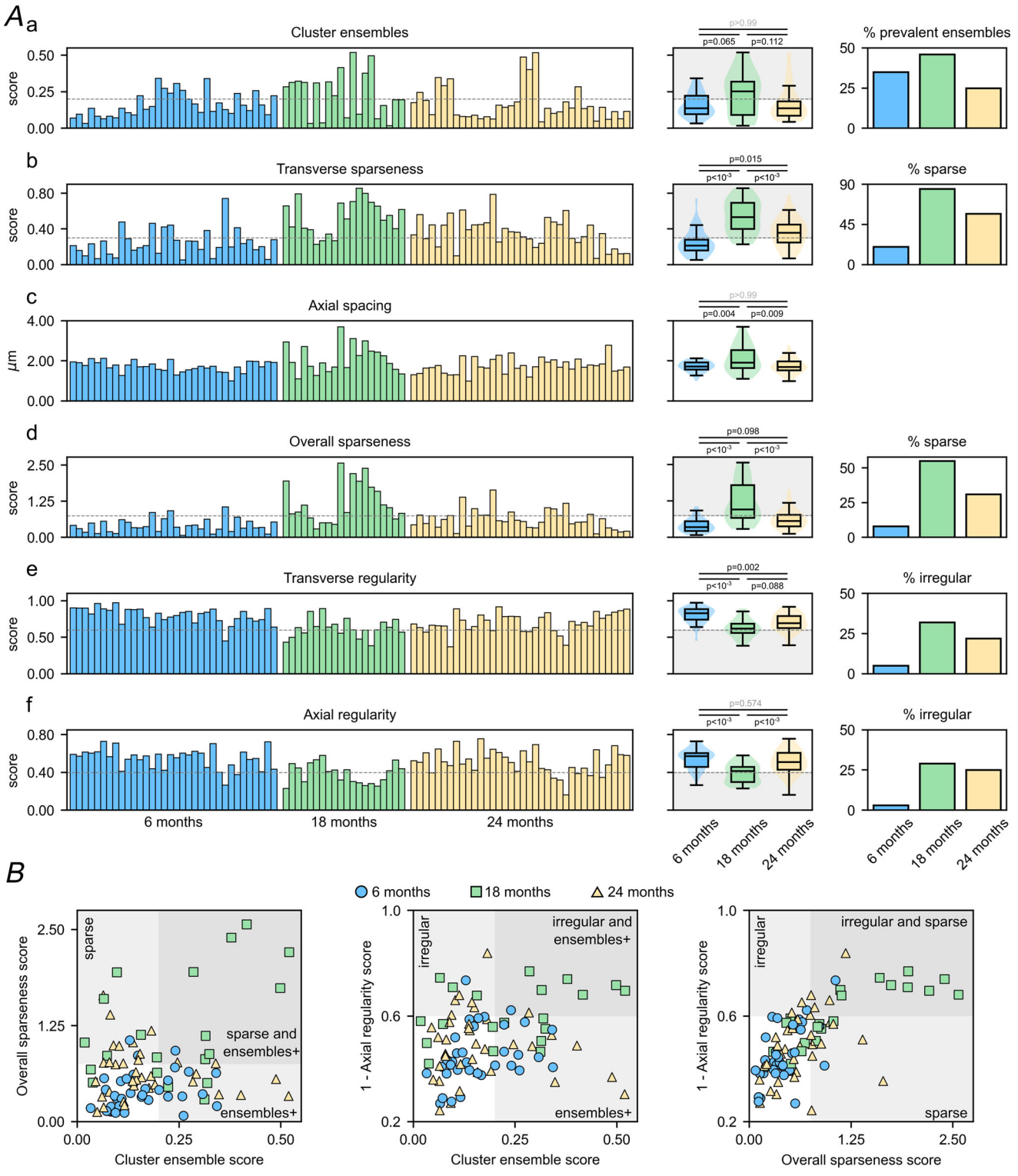

Figure 8. Summary of structural phenotype analysis
A, image-by-image scores for the various structural metrics, and summary of the distributions grouped by age, with the probability of animals meeting the threshold (indicated by the dotted line and the grey shaded area). Data are presented across age; 6 months (blue; $N = 6$ animals; $n = 23$ cells and $n = 34$ images), 18 months (green; $N = 5$ animals; $n = 14$ cells and $n = 20$ images) and 24 months (orange; $N = 6$ animals; $n = 21$ cells and $n = 36$ images). *B*, correlations between the primary structural scores.

both aged groups compared to the 6-month group (5% in the 6-month group, 32% in the 18-month group and 22% at the 24-month group).

Across all metrics the 18-month group displayed the largest variability and the highest probability of remodelling, with the 24-month group exhibiting either partial or full recovery. Correlating the various scores with each other further revealed the combined features of remodelling (Fig. 8*B*). The 18-month group consistently exhibited the highest probability of finding cells that surpassed the thresholds for multiple metrics concurrently, for example an individual image being both sparse and irregular, whereas the other two groups tended to produce cells that surpassed the threshold in only one metric.

Discussion

Summary of major findings

In this study we have characterized the properties of calcium sparks and RyR clusters in isolated ventricular myocytes from a sedentary model of ageing in rats at three different age points (6, 18 and 24 months). Generally the aged cohorts were associated with an increased probability of structural remodelling corresponding to fragmentation, sparseness and irregularity (Fig. 8 and Figs A6–A9). These structural changes accompanied a greater morphological change in spontaneous calcium spark response upon the application of ISO with age. Both aged groups exhibited a high spontaneous spark rate compared to the 6-month group, and the 24-month group exhibited the most substantial response to ISO.

Structural phenotypes

Our analyses focused on cluster structure and inter-cluster relationships, which revealed various structural phenotypes that were characterized by our structural metrics: 'typical' cells contained medium-sized clusters and a clear and robust transverse and axial structure; 'high degree of cluster ensembles' cells that were characterized by fragmentated-like clusters; 'sparse' cells with large separation between clusters at the larger scale; and 'disorganized' cells that were characterized by an irregular transverse and axial structure.

Many overall differences between the groups were underpinned by an increase in interanimal variability with age, mixing more typical and remodelled phenotypes. Generally there was an increased propensity for animals that contained cells with high cluster ensemble scores (indicating fragmentation), sparsity scores and irregular structure scores with age, with a reduction in those displaying typical and robust cell types. The 6-month group contained primarily typical and robust cell types, with little representation from disorganized, sparse or fragmented cells. The 18-month group exhibited over-representation of cells that contained many cluster ensembles, were sparse and/or exhibited a high degree of irregularity. The 24-month group was more mixed between typical and robust cell types and those associated with remodelling. Transverse spacing was largely preserved across age, with larger edge-to-edge differences at 18 months due to a reduction in cluster height, whereas variability in the coarse-grained axial spacing was generally increased in the aged groups, underpinned by a redistribution of the clusters rather than changes to cluster structure, correlating with the more disorganized phenotypes.

Biphasic age-dependent progression of remodelling

Three age points were chosen for the present study to provide insight into the continuum of remodelling that occurs during the ageing process; indeed pilot data indicated an acceleration of remodelling by age 24 months. Counter to our expectations we report, to our knowledge for the first time, a biphasic progression of multiple properties with age, exhibiting significant remodelling between 6 and 18 months and then partial or full recovery by 24 months. Generally the biphasic changes were characterized by the emergence and high representation of animals that contained cells with a high prevalence of cluster ensembles, sparsity and/or disorganized RyR clusters in the 18-month group. The extent of their representation was reduced at 24 months but remained present, leaving both aged groups to exhibit a degree of remodelling compared to the 6-month controls. Primarily small-scale remodelling (i.e. fragmentation) was biphasic, with partial recovery in the 24-month group, whereas larger-scale features (axial distances, sparseness and general disorder) were generally remodelled in both aged groups compared to the 6-month group, although often still showing a small degree of partial recovery at 24 months.

The potential role of survivor bias may confound these observations and leads to two possible interpretations for these results: we have observed either a genuine process of remodelling and partial recovery with age, or the divergence of 'healthy' and 'unhealthy' aged groups wherein the 18-month group is largely populated by the 'unhealthy' animals that needed to be culled at that time. The larger the contribution of this potential survivor bias, the more suitable the second explanation becomes. We note that not all animals in the 18-month group were selected based on animal husbandry concerns, and that many of the husbandry concerns that led to the selection of animals being culled rather than further aged did not necessarily correlate directly with general

health (e.g. long nails). Nevertheless we cannot rule out the contribution of survivor bias to our observations of the biphasic progression of remodelling with age. It is therefore highly likely that both interpretations are valid to an extent; that is there is a degree of remodelling and recovery, while individuals also age with different degrees of health. We are confident that all remodelling observed between either aged group and the 6-month controls represents a real and meaningful change in the structure–function relationships underpinning calcium handling during sedentary ageing. Whether remodelling occurs and then partially reverses in individuals, or whether our observations are primarily explained by divergence of groups, needs further investigation.

Some observed features support the interpretation of a genuinely biphasic remodelling process. For example we observed similar features to those reported by Caldwell et al. (2024), who explored recovery of the t-system following heart failure. Heart failure was associated with a high degree of detubulation, whereas in recovery t-system density was largely restored but the underlying structure remained disorganized compared to control. This is analogous to our observations of substantially increased prevalence of cluster ensembles at 18 months and a reduction at 24 months but an increase in the disorder and dispersion of clusters at the larger scale.

It is therefore likely that some form of partial recovery occurs between these two age points, which may be related to the increased sensitivity to ISO at 24 months. We therefore argue that future studies should consider multiple age points to verify or refute our observations and provide further insight into the potentially interacting and compensatory roles of structural and functional remodelling during the progression of ageing.

Sympathetic regulation

ISO had no significant impact upon calcium spark morphology in the young 6-month animals but did have a noticeable effect with age, with the largest impact on spark size in the 24-month group compared to the basal conditions. Shen et al. (2022) noted that exposure of ISO to a fragmented RyR cluster pattern was found to increase calcium spark fidelity, improving intercluster communication, with larger calcium sparks recorded. This is supported by Hou et al. (2023), who observed β-adrenergic stimulation increasing RyR recruitment to enable calcium spark formation, and Litwin et al. (2000), who noted β-adrenergic stimulation of left ventricular myocytes in a rabbit myocardial infarction (MI) model of heart failure improved calcium synchronization.

In our data we evaluated calcium spark morphology in the presence of ISO in a different subset of cells from which RyR structural morphology was derived, and so no conclusions can be drawn in a correlative manner. However we noted that fragmentation was most apparent at 18 months, but the greatest change in calcium spark mass was evident at 24 months. One consideration could be an additional regulation of the RyR channel at 24 months, which was not evident at 18 months, with response to ISO being determined by factors additional to RyR cluster pattern. Within the failing heart, for example, hyperphosphorylation is present (Sheard et al., 2019) and is suggested to drive dispersion of RyR through the CaMKII and PKA pathways, leading to an increase in calcium spark amplitude and FWHM (Shen et al., 2022). As such, phosphorylation, alongside RyR orientation, is considered determinants of calcium signalling within heart failure (Hernández Mesa et al., 2022). Blockade of β-adrenergic stimulation preserved calcium functionality in a rodent model of pulmonary artery hypertension (Fowler et al., 2018), with inhibition of the PKA/CaMKII pathway in a rodent heart failure model leading to the RyR cluster pattern and calcium spark kinetics being restored, akin to our 24-month animals, proposing an ability of the ageing heart, unlike the failing heart, to internally regulate. The exact mechanism of action underlying the increased response to ISO with age requires further study, with an increased number of small RyR clusters being associated with increased β-adrenergic response but by no means is causation suggested.

Comparisons to heart failure remodelling

Remodelling of the heart at multiple scales is associated with many cardiac conditions, notably including the various presentations of heart failure. Although the ageing heart and the failing heart are distinct, observations can be drawn between features of the two. Broadly, some aged hearts may present similar features to heart failure, such as reduced cardiac output and increased vulnerability to arrhythmia, including sudden cardiac death, which may be underpinned by similar features of structural and functional remodelling at multiple scales, including dilatation, hypertrophy, increased spatial heterogeneity, prolongation of the action potential, abbreviation of the intracellular calcium transient and subcellular structural remodelling of calcium handling apparatus. Thus aged hearts that present these features may be comparable to heart failure but with distinct aspects of the phenotype.

Our observations support the emergence of some similar features in ageing and heart failure at the sub-cellular level. We observed a substantial increase in interanimal variability with age, and it is those that displayed markedly different properties to the 6-month group that exhibited broadly similar characteristics to heart failure. Previous studies have revealed that calcium transient kinetics are altered and cell-wide calcium desynchrony is apparent in heart failure (Fowler et al.,

2020; Louch et al., 2004), which have been correlated with disorganization of the t-system and alteration in RyR cluster pattern, including increased fragmentation (Dibb et al., 2022; Galice et al., 2018; Hurley et al., 2023; Ibrahim et al., 2011; Kolstad et al., 2018; Sheard et al., 2022; Soeller et al., 2009; Song et al., 2006; Walker et al., 2014). At 18 and 24 months of age there was an increased propensity for animals that contained cells with high fragmentation and irregular global RyR cluster distribution. In Kolstad et al. (2018) a rat aortic-banded model of heart failure revealed the fragmentation of inter-cluster distances that was considered the predominant driver for decreased calcium spark fidelity, with smaller RyR clusters leading to calcium leak. Comparatively in our 18-month animals, where fragmentation was most apparent, calcium spark amplitude and frequency increased and FWHM decreased, with the converse observed at 24 months. This suggests that across ageing, alterations in RyR cluster pattern within the junctional dyad are not the sole determinant of calcium spark fidelity. This is unlike that proposed in the failing heart. Instead moderate changes in RyR gating could be the principal determinant for altered calcium spark morphology as age increases (Cannell et al., 2013), with a single spark release having minimal dependence upon RyR organization (Hou et al., 2023). We report a partial recovery of FWHM/amplitude at 24 months, with an increase in the median N_{RyR}, comparatively aligning closer with the 6-month baseline than the 18-month mid-point. This suggests that the heart has undergone a compensatory mechanism that is lacking in heart failure.

Furthermore depletion of the SR calcium store through calcium leak (Boyden & Smith, 2018; Dridi et al., 2020), altered calcium spark morphology and a reduction in calcium transient kinetics have been recorded in heart failure (Fowler et al., 2020; Hurley et al., 2023; Louch et al., 2013). Combined these changes can lead to the generation of delayed afterdepolarization and ultimately to the development of arrhythmia (Waddell et al., 2023). These aspects were not investigated in our present study, but the correlation of related structural features between ageing and heart failure that we observe implies a potential relevance that should direct future investigations.

Limitations

This study has several methodological limitations that should be considered for interpretation of the findings. First the temporal resolution achievable with confocal spinning disk imaging was insufficient to resolve the full time course of individual calcium sparks. Because sparks could arise and dissipate within a single acquisition frame, their true durations remain unknown. Spatial precision was also constrained by the use of a diffusive calcium-indicator dye, which may have introduced signal blurring and limited the fidelity of local calcium-release measurements. Moreover our analyses were restricted to spontaneous Ca^{2+} spark kinetics measured from a small subcellular region, capturing only part of the broader physiological behaviour expected *in vivo* (Cheng & Lederer, 2008). To minimize artefacts we applied stringent exclusion criteria, as detailed in Methods section, to remove spurious or out-of-focus spark detections (Hurley et al., 2021), although this necessarily reduced the number of analysable events. Frame rate varied between the 6-month control and aged groups, with the slower frame rate accounting for the lower signal-to-noise ratio with age. To calculate the FWHM the peak of the calcium spark needs to be captured. We are confident that this is done across the frame rates used, with the use of the analysis package xyspark, and our subsequent filtering applied to ensure that only in-plane calcium sparks, following a Gaussian fit of fluorescence distribution, were included. However due to differences in frame rate comparison of calcium spark morphology across age has not been undertaken.

Limitations also arise from the expansion-microscopy approach. Although 4× EExM achieved an in-plane resolution of <40 nm and an axial resolution of <90 nm (Sheard et al., 2022), these values remain poorer than the dimensions of individual RyR puncta, meaning that cluster-pattern measurements should be regarded as estimates rather than direct representations of native ultrastructure. This consideration, however, does not affect comparisons between groups and would manifest only as a small error in the estimation of absolute numbers of RyRs per cluster. The extent to which the expansion process is fully isotropic remains a matter of ongoing discussion. Prior characterization within ventricular cardiomyocytes using identical chemistry, instrumentation and laboratory conditions supports the reliability of the method as applied here (Sheard et al., 2019), with fluorospheres used to define the point spread function within a hydrogel to quantify the level of optical diffraction present. We were unable to perform correlative functional–structural imaging in the present study; however Hou et al. (2023) reported that RyR mean size was unaffected by ISO treatment in a correlative framework, suggesting that major functional–structural discrepancies are unlikely when evaluating RyR structure obtained under calcium conditions, with Ca^{2+} spark function obtained in presence of ISO. As with all post-fixation approaches the potential impact of 2% fixation on RyR cluster organization is unknown, particularly in light of previous observations of dynamic RyR redistribution at the cell periphery in live-cell imaging (Hiess et al., 2018); however it is important to note that our RyR datasets were from internal dyads. The RyR antibody used here has been previously validated for DNA-PAINT (Jayasinghe

et al., 2018); however antibody size and linker error remain inherent limits of immuno-based super-resolution imaging. Furthermore we did not assess additional regulatory proteins involved in calcium signalling, which constrains interpretation of the molecular context of the observed changes, nor was t-system density directly characterized, which may correlate substantially with RyR remodelling.

Aspects of the animal model introduce further limitations. The use of a sedentary model may restrict the generalizability of the findings to animals experiencing different physiological loads or activity levels.

The structural phenotyping metrics that were developed in this study were rather simplistic and crude. Despite this they did provide a useful and visually validated approach to quantify cells from each age group. The cluster ensemble score did exhibit a small correlation with the resolution of the original image (higher-resolution images were more able to resolve separated localized clusters), which could impact our analyses. However the range of cluster ensemble scores was observed across almost all resolutions, and the distribution of age group and resolution did not correlate. Moreover the two cells with the lowest resolution and score were from the 18-month group, which would therefore potentially underestimate the significantly increased degree of cluster ensembles in that group compared to the other two groups. Nevertheless it is worth considering that our results will be influenced by resolution. All other structural phenotype metrics were derived from the coarse-grained model, which was therefore not sensitive to the original image resolution, although incurs the implicit limitations of the coarse-graining approach.

Conclusion

We have characterized calcium spark morphology in response to β-adrenergic stimulation and RyR cluster properties in a model of sedentary ageing at three age points corresponding to young adults (6 months) and aged adults (18 and 24 months). Calcium spark properties were unaltered in the young adults upon β-adrenergic stimulation but remodelled in both ageing groups, with the greatest change exhibited within the 24-month group. Across age remodelling of multiple properties of RyR cluster and intercluster structure was noticeable, with many showing a biphasic response, exhibiting recovery between 18 and 24 months. Primarily the 18-month group contained a substantial increase in fragmentation compared to the 6-month group, and the 24-month group exhibited less fragmentation but more global disorder and remained significantly remodelled compared to the 6-month group. Remodelling and partial recovery were underpinned by an increase in inter-cellular and interanimal variability in both age groups, indicating a diverse population of healthy and less healthy subjects. Features of remodelling were analogous to heart failure but with a distinct characteristic of the phenotype. Our results indicate that functional and structural remodelling combine to explain abbreviations in subcellular calcium handling associated with age, and that intercluster relationships may be more important than overall cluster size.

Appendix

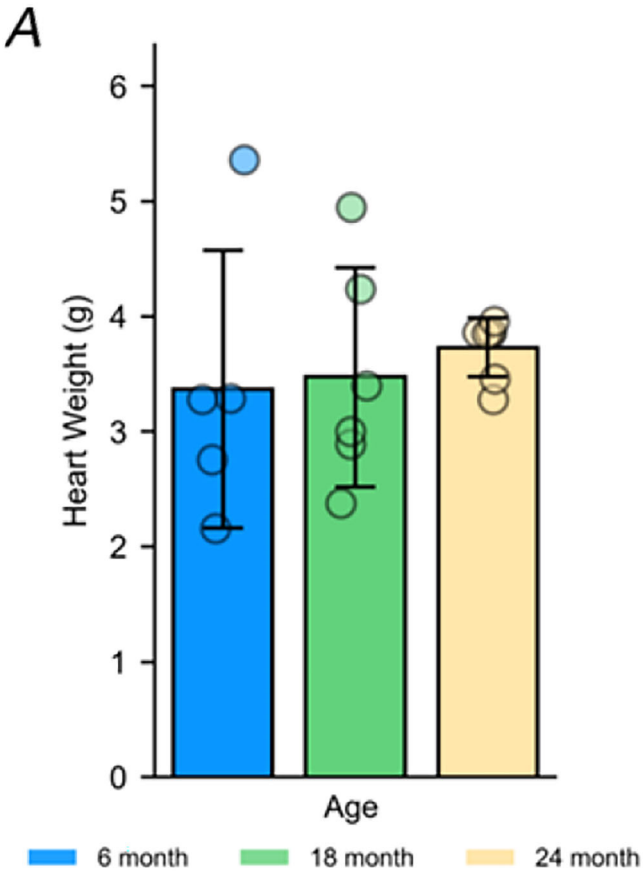

Figure A1. Absolute heart weight
A, the individual heart weight of each adult male Wistar rat across the three age points: 6 months (blue; $N = 5$), 18 months (green; $N = 6$) and 24 months (orange; $N = 7$), with mean ± SD.

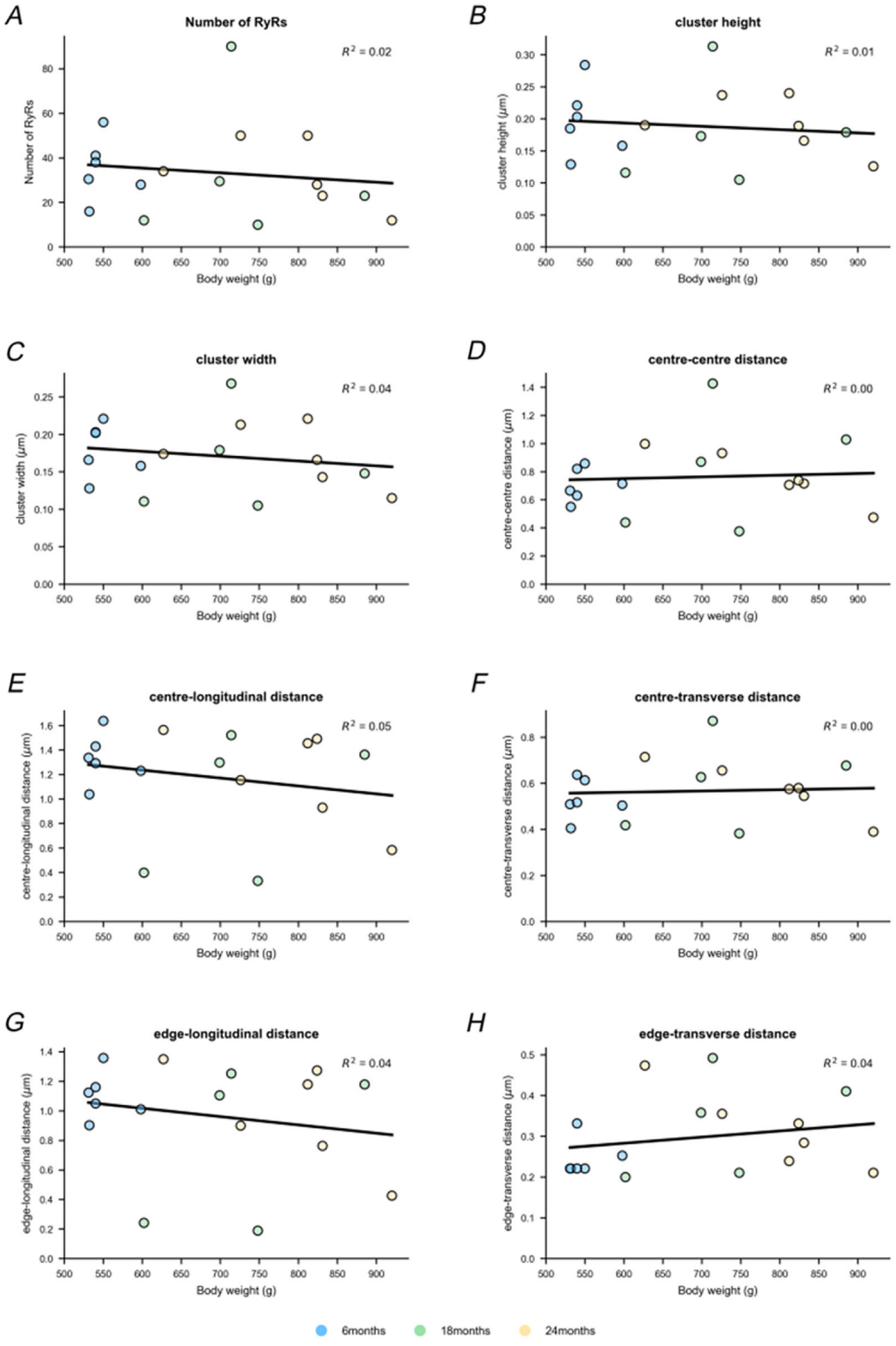

Figure A2. Correlation between body weight and measures of ryanodine receptor (RyR) cluster pattern
The individual body weight of each adult male Wistar rat across the three age points: 6 months (blue; $N = 8$), 18 months (green; $N = 6$) and 24 months (orange; $N = 7$) were plotted against measures of RyR cluster pattern, with a regression value calculated from a regression analysis undertaken in Python. Measures of RyR cluster pattern were (*A*) number of RyR puncta per cluster, (*B*) cluster height, (*C*) cluster width, (*D*) centre-to-centre distance between RyR clusters, (*E*) centre-to-centre distance in the longitudinal direction between RyR clusters, (*F*) centre-to-centre distance between RyR clusters in the transverse direction, (*G*) edge-to-edge distance between RyR clusters in the longitudinal direction and (*H*) edge-to-edge distance between RyR clusters in the transverse direction.

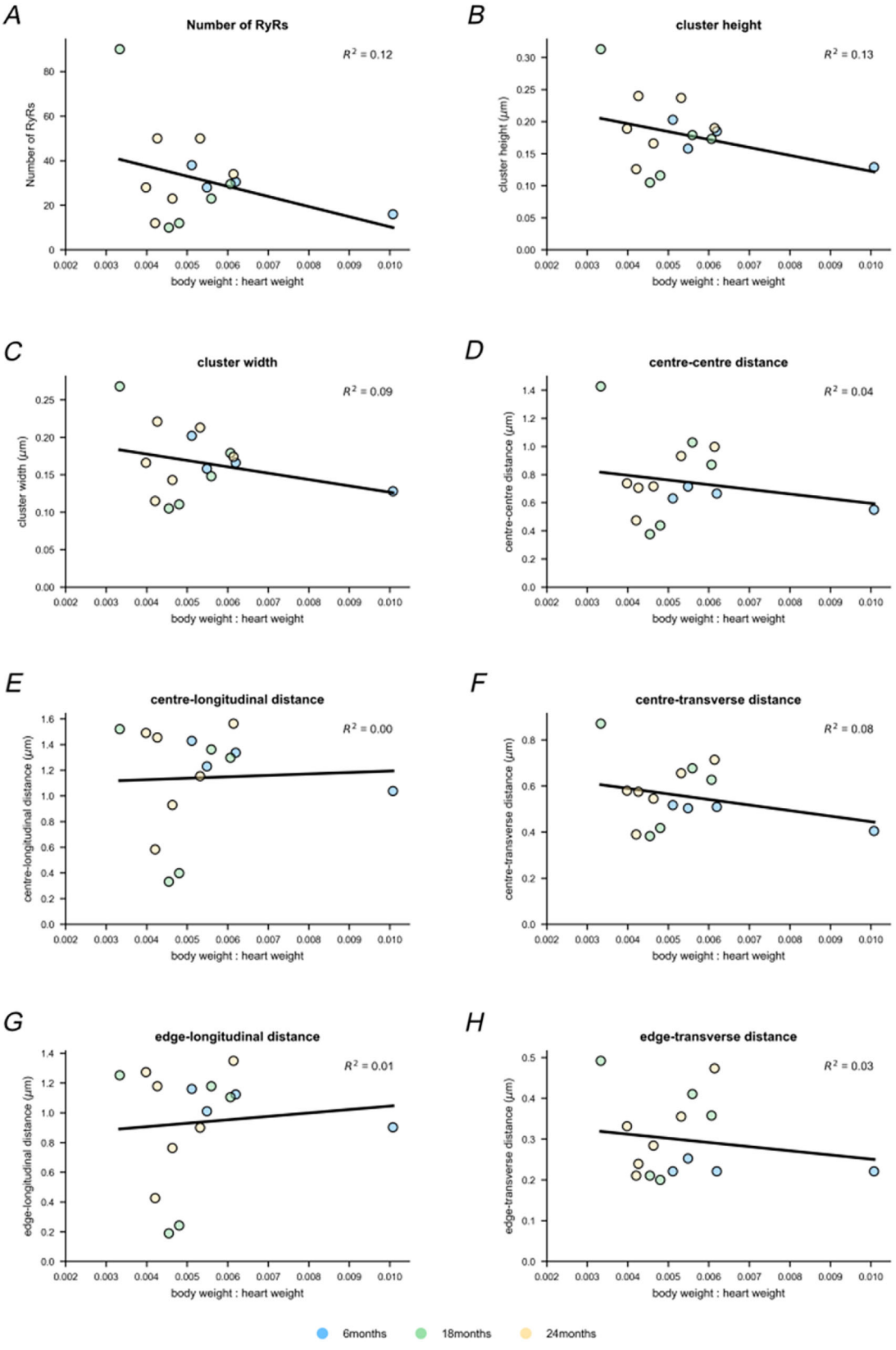

Figure A3. Correlation between the body weight to heart weight ratio and measures of ryanodine receptor (RyR) cluster pattern
The individual body weight of each adult male Wistar rat was quantified as a ratio in respect to the animal's corresponding heart weight across the three age points: 6 months (blue; $N = 8$), 18 months (green; $N = 6$) and

24 months (orange; $N = 7$). This ratio was plotted against measures of RyR cluster pattern, with a regression value calculated from a regression analysis undertaken in Python. Measures of RyR cluster pattern were (*A*) number of RyR puncta per cluster, (*B*) cluster height, (*C*) cluster width, (*D*) centre-to-centre distance between RyR clusters, (*E*) centre-to-centre distance in the longitudinal direction between RyR clusters, (*F*) centre-to-centre distance between RyR clusters in the transverse direction, (*G*) edge-to-edge distance between RyR clusters in the longitudinal direction and (*H*) edge-to-edge distance between RyR clusters in the transverse direction.

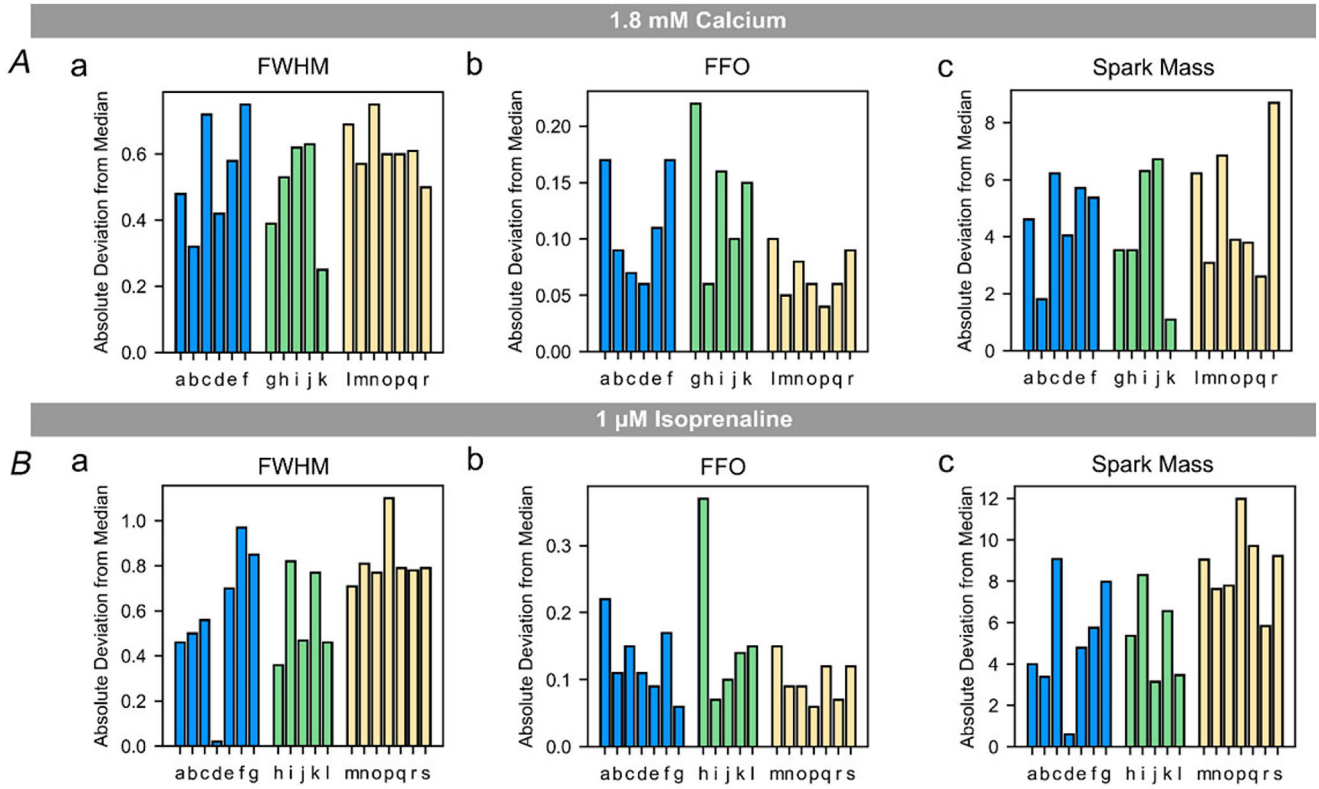

Figure A4. Variability within measures of calcium spark morphology in 1.8 mM calcium and 1 µM isoprenaline conditions
Isolated ventricular cardiomyocytes from a male Wistar rat model of sedentary ageing at 6 months (blue), 18 months (green) and 24 months (orange). Cardiomyocytes were loaded with 5 µM Fluo-4 AM, and spontaneous calcium spark events were recorded using a confocal spinning disk microscope and analysed using FIJI *ImageJ*, xyspark plug-in. Absolute deviation from the age-grouped median was calculated on an animal-to-animal basis using *SPSS*. This was undertaken for full-width at half maximum in presence of calcium (6 months: $N = 6$; 18 months: $N = 5$; 24 months: $N = 7$) (*Aa*) and isoprenaline (6 months: $N = 7$; 18 months: $N = 5$; 24 months: $N = 7$) (*Ba*), amplitude as determined by fluorescence intensity according to F/F0 in presence of calcium (*Ab*) and isoprenaline (*Bb*) and spark mass as a factor of FWHM and F/F0 combined in presence of calcium (*Ac*) and isoprenaline (*Bc*).

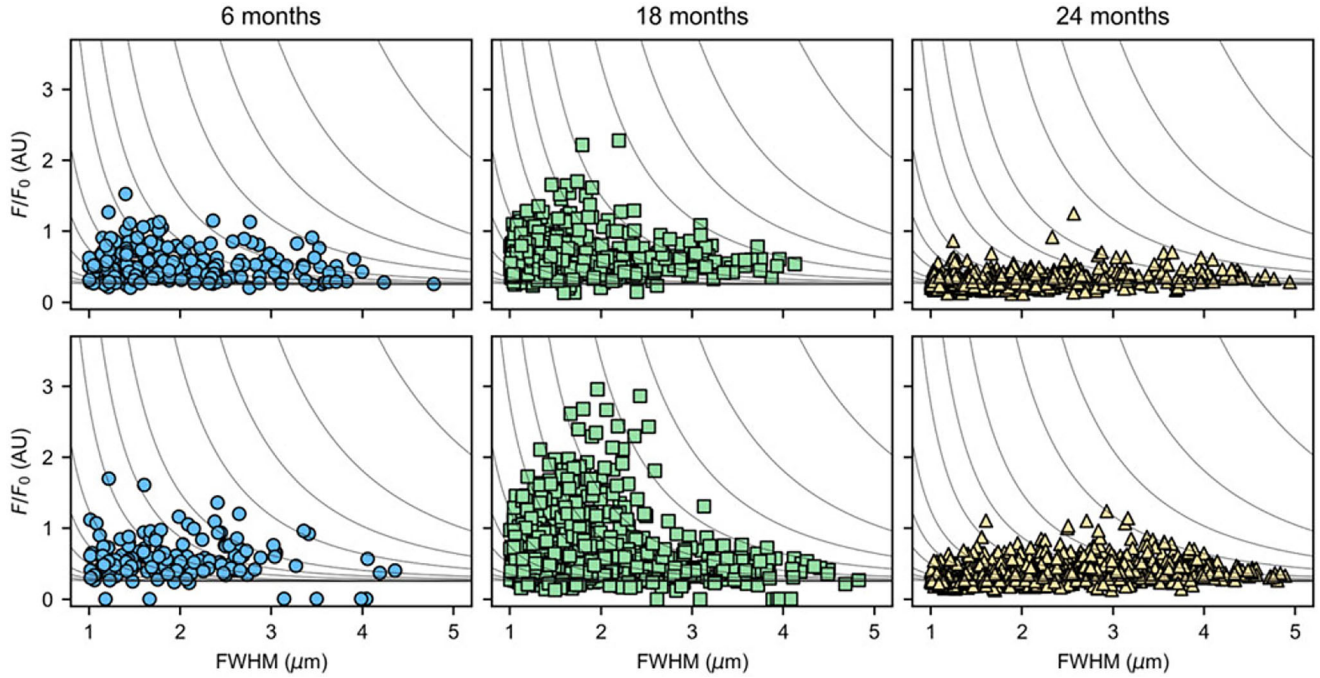

Figure A5. Correlation of full-width at half maximum (FWHM) and amplitude for calcium sparks
Upper panel is 1.8 mM calcium control, and the lower panel is 1 μM isoprenaline (ISO). Grey lines indicate contours of constant spark mass.

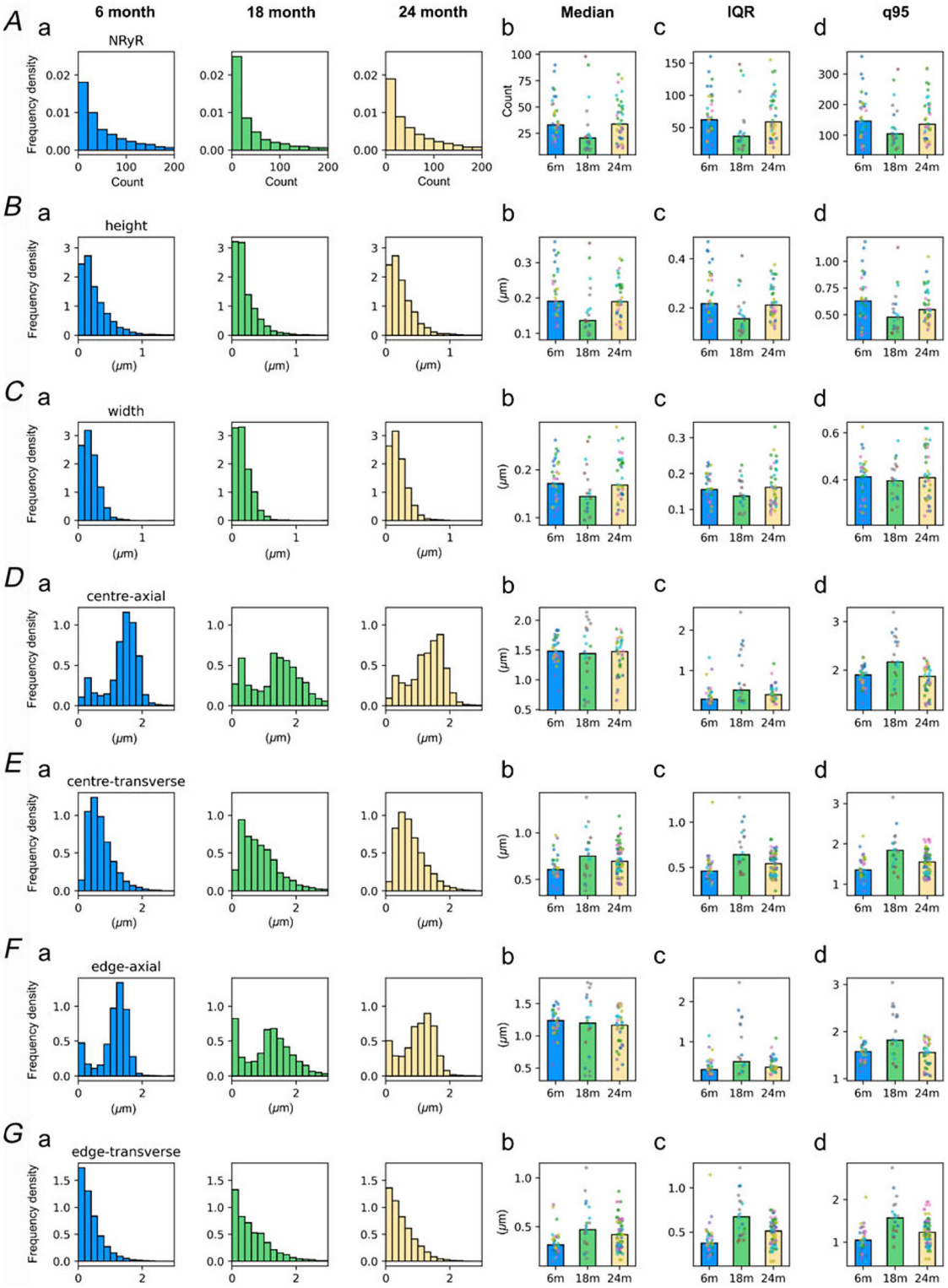

Figure A6. Summary of properties of the ryanodine receptor (RyR) cluster pattern across age
Cluster properties across age at 6 months (blue; $N = 6$), 18 months (green; $N = 5$) and 24 months (orange; $N = 6$). Clusters are characterized by (*A*) number of RyR per cluster (NRyR), (*B*) cluster height, (*C*) cluster width, (*D*) centre-to-centre axial distance between clusters, (*E*) centre-to-centre transverse distance between clusters, (*F*) edge-to-edge axial distance between clusters, (*G*) edge-to-edge transverse distance between clusters as illustrated for each variable by histograms for (*a*) 6 months (blue), 18 months (green) and 24 months (orange) and plots with (*b*) median, (*c*) interquartile range and (*d*) 95th percentile, all with individual data points mapped.

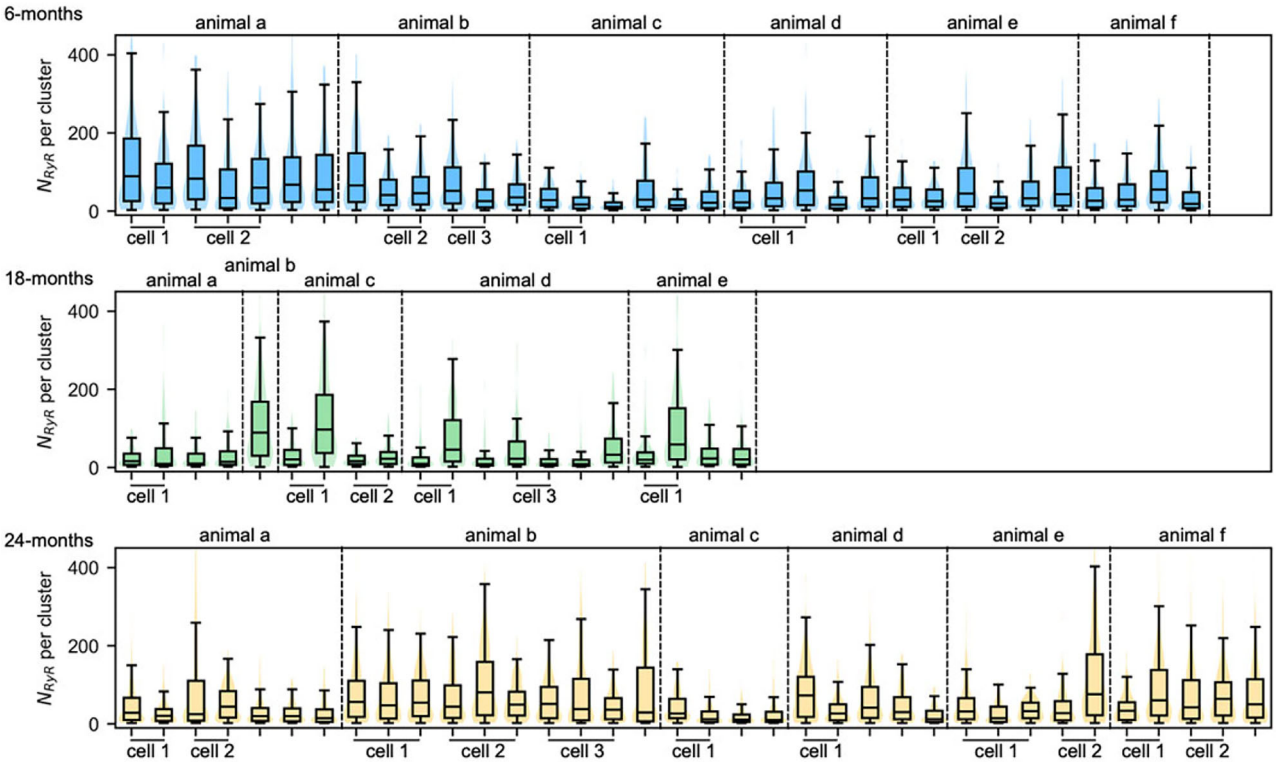

Figure A7.
Intercellular and interanimal variability in cluster size.

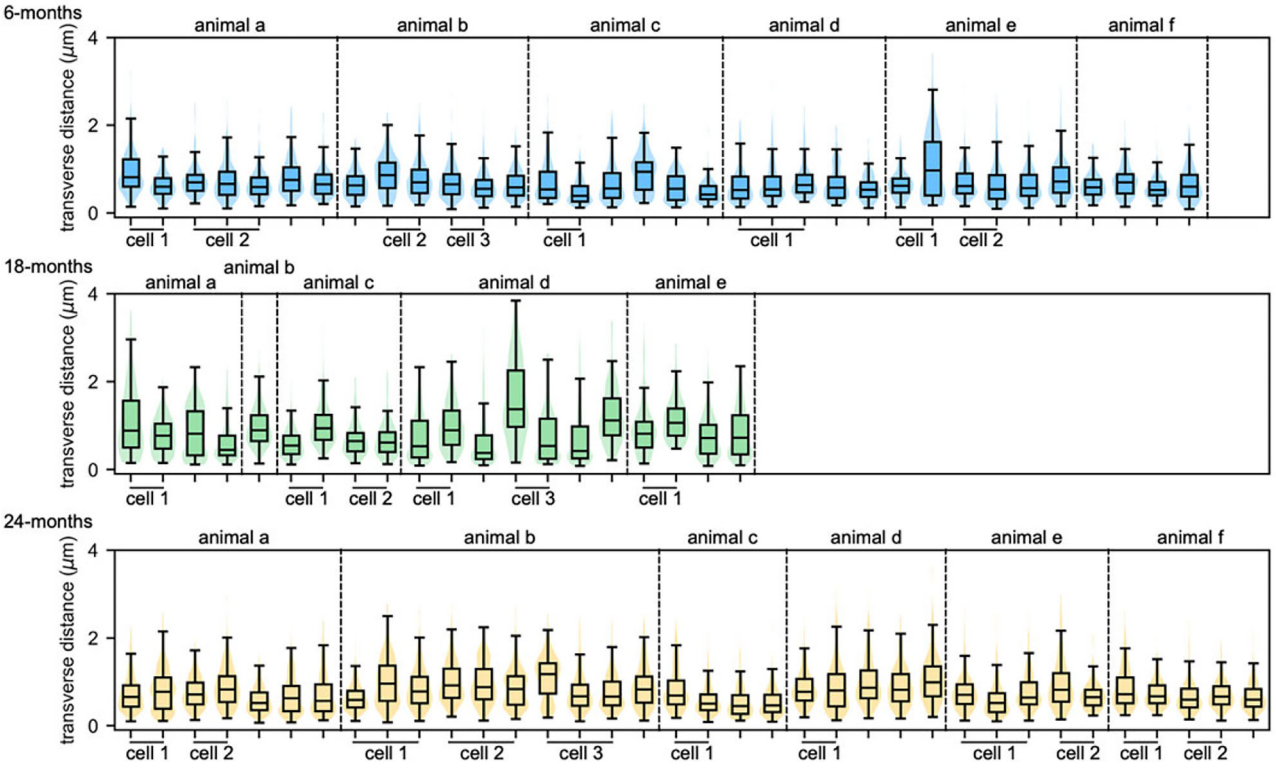

Figure A8.
Intercellular and interanimal variability in centre-to-centre intercluster transverse distances.

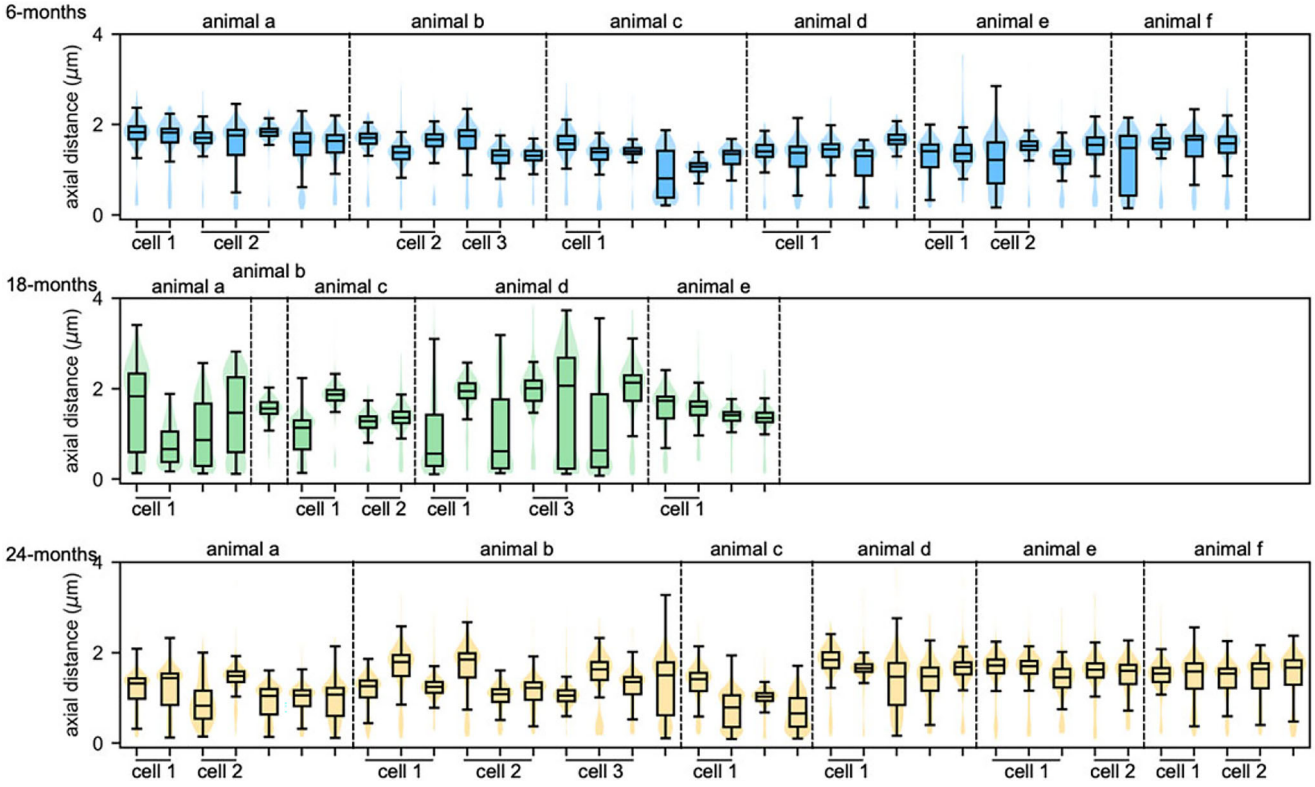

Figure A9.
Intercellular and interanimal variability in centre-to-centre intercluster axial distances.

References

Aistrup, G. L., Arora, R., Grubb, S., Yoo, S., Toren, B., Kumar, M., Kunamalla, A., Marszalec, W., Motiwala, T., Tai, S., Yamakawa, S., Yerrabolu, S., Alvarado, F. J., Valdivia, H. H., Cordeiro, J. M., Shiferaw, Y., & Wasserstrom, J. A. (2017). Triggered intracellular calcium waves in dog and human left atrial myocytes from normal and failing hearts. *Cardiovascular Research*, **113**(13), 1688–1699.

Baddeley, D., Jayasinghe, I., Lam, L., Rossberger, S., Cannell, M. B., & Soeller, C. (2009). Optical single-channel resolution imaging of the ryanodine receptor distribution in rat cardiac myocytes. *Proceedings of the National Academy of Sciences of the United States of America*, **106**(52), 22275–22280.

Bhatnagar, P., Wickramasinghe, K., Williams, J., Rayner, M., & Townsend, N. (2015). The epidemiology of cardiovascular disease in the UK 2014. *Heart*, **101**(15), 1182–1189.

Boyden, P. A., & Smith, G. L. (2018). Ca^{2+} leak—What is it? Why should we care? Can it be managed? *Heart Rhythm*, **15**(4), 607–614.

Brette, F., Rodriguez, P., Komukai, K., Colyer, J., & Orchard, C. H. (2004). beta-adrenergic stimulation restores the Ca transient of ventricular myocytes lacking t-tubules. *Journal of Molecular and Cellular Cardiology*, **36**(2), 265–275.

Caldwell, J. L., Clarke, J. D., Smith, C. E. R., Pinali, C., Quinn, C. J., Pearman, C. M., Adomaviciene, A., Radcliffe, E. J., Watkins, A., Horn, M. A., Bode, E. F., Madders, G. W. P., Eisner, M., Eisner, D. A., Trafford, A. W., & Dibb, K. M. (2024). Restoring atrial T-tubules augments systolic Ca upon recovery from heart failure. *Circulation Research*, **135**(7), 739–754.

Cannell, M. B., Kong, C. H. T., Imtiaz, M. S., & Laver, D. R. (2013). Control of sarcoplasmic reticulum Ca^{2+} release by stochastic RyR gating within a 3D model of the cardiac dyad and importance of induction decay for CICR termination. *Biophysical Journal*, **104**(10), 2149–2159.

Cheng, H., Lederer, M. R., Lederer, W. J., & Cannell, M. B. (1996). Calcium sparks and $[Ca^{2+}]$i waves in cardiac myocytes. *American Journal of Physiology-Cell Physiology*, **270**(1 Pt 1), C148–C159.

Cheng, H., & Lederer, W. J. (2008). Calcium sparks. *Physiological Reviews*, **88**(4), 1491–1545.

Colman, M. A. (2019). Arrhythmia mechanisms and spontaneous calcium release: Bi-directional coupling between re-entrant and focal excitation. *PLoS Computational Biology*, **15**(8), e1007260.

Costantino, S., Paneni, F., & Cosentino, F. (2016). Ageing, metabolism and cardiovascular disease. *The Journal of Physiology*, **594**(8), 2061–2073.

Dai, D.-F., Chen, T., Johnson, S. C., Szeto, H., & Rabinovitch, P. S. (2012). Cardiac aging: From molecular mechanisms to significance in human health and disease. *Antioxidants & Redox Signaling*, **16**(12), 1492–1526.

Dibb, K. M., Louch, W. E., & Trafford, A. W. (2022). Cardiac transverse tubules in physiology and heart failure. *Annual Review of Physiology*, **84**, 229–255.

Dridi, H., Kushnir, A., Zalk, R., Yuan, Q., Melville, Z., & Marks, A. R. (2020). Intracellular calcium leak in heart failure and atrial fibrillation: A unifying mechanism and therapeutic target. *Nature Reviews Cardiology*, **17**(11), 732–747.

Fogg, C., England, T., Zhu, S., Jones, J., de Lusignan, S., Fraser, S. D. S., Roderick, P., Clegg, A., Harris, S., Brailsford, S., Barkham, A., Patel, H. P., & Walsh, B. (2024). Primary and secondary care service use and costs associated with frailty in an ageing population: Longitudinal analysis of an English primary care cohort of adults aged 50 and over, 2006–2017. *Age and Ageing*, **53**(2), afae010.

Fowler, E. D., Drinkhill, M. J., Norman, R., Pervolaraki, E., Stones, R., Steer, E., Benoist, D., Steele, D. S., Calaghan, S. C., & White, E. (2018). Beta1-adrenoceptor antagonist, metoprolol attenuates cardiac myocyte Ca^{2+} handling dysfunction in rats with pulmonary artery hypertension. *Journal of Molecular and Cellular Cardiology*, **120**, 74–83.

Fowler, E. D., Wang, N., Hezzell, M., Chanoit, G., Hancox, J. C., & Cannell, M. B. (2020). Arrhythmogenic late Ca^{2+} sparks in failing heart cells and their control by action potential configuration. *Proceedings of the National Academy of Sciences of the United States of America*, **117**(5), 2687–2692.

Galice, S., Xie, Y., Yang, Y., Sato, D., & Bers, D. M. (2018). Size matters: Ryanodine receptor cluster size affects arrhythmogenic sarcoplasmic reticulum calcium release. *Journal of the American Heart Association*, **7**(13), e008724.

Greiser, M., Kerfant, B.-G., Williams, G. S. B., Voigt, N., Harks, E., Dibb, K. M., Giese, A., Meszaros, J., Verheule, S., Ravens, U., Allessie, M. A., Gammie, J. S., van der Velden, J., Lederer, W. J., Dobrev, D., & Schotten, U. (2014). Tachycardia-induced silencing of subcellular Ca^{2+} signaling in atrial myocytes. *Journal of Clinical Investigation*, **124**(11), 4759–4772.

Hajduk, A. M., & Chaudhry, S. I. (2016). Sedentary behavior and cardiovascular risk in older adults: A scoping review. *Current Cardiovascular Risk Reports*, **10**(1), 5.

Hartigan, J. A., & Hartigan, P. M. (1985). The dip test of unimodality. *The Annals of Statistics*, **13**(1), 70–84.

Hatch, F., Lancaster, M. K., & Jones, S. A. (2011). Aging is a primary risk factor for cardiac arrhythmias: Disruption of intracellular Ca^{2+} regulation as a key suspect. *Expert Review of Cardiovascular Therapy*, **9**(8), 1059–1067.

Hernández Mesa, M., van den Brink, J., Louch, W. E., McCabe, K. J., & Rangamani, P. (2022). Nanoscale organization of ryanodine receptor distribution and phosphorylation pattern determines the dynamics of calcium sparks. *PLoS Computational Biology*, **18**(6), e1010126.

Hiess, F., Detampel, P., Nolla-Colomer, C., Vallmitjana, A., Ganguly, A., Amrein, M., ter Keurs, H., Benítez, R., Hove-Madsen, L., & Chen, S. R. W. (2018). Dynamic and irregular distribution of RyR clusters in the periphery of live ventricular myocytes. *Biophysical Journal*, **114**(2), 343–354.

Hou, Y., Laasmaa, M., Li, J., Shen, X., Manfra, O., Nordén, E. S., Le, C., Zhang, L., Sjaastad, I., Jones, P. P., Soeller, C., & Louch, W. E. (2023). Live-cell photoactivated localization microscopy correlates nanoscale ryanodine receptor configuration to calcium sparks in cardiomyocytes. *Nature Cardiovascular Research*, **2**(3), 251–267.

Huff, J. (2015). The Airyscan detector from ZEISS: Confocal imaging with improved signal-to-noise ratio and super-resolution. *Nature Methods*, **12**, i–ii.

Hurley, M. E., Sheard, T. M. D., Norman, R., Kirton, H. M., Shah, S. S., Pervolaraki, E., Yang, Z., Gamper, N., White, E., Steele, D., & Jayasinghe, I. (2021). A correlative super-resolution protocol to visualise structural underpinnings of fast second-messenger signalling in primary cell types. *Methods*, **193**, 27–37.

Hurley, M. E., White, E., Sheard, T. M. D., Steele, D., & Jayasinghe, I. (2023). Correlative super-resolution analysis of cardiac calcium sparks and their molecular origins in health and disease. *Open Biology*, **13**(5), 230045.

Ibrahim, M., Gorelik, J., Yacoub, M. H., & Terracciano, C. M. (2011). The structure and function of cardiac t-tubules in health and disease. *Proceedings of the Royal Society B: Biological Sciences*, **278**(1719), 2714–2723.

Jayasinghe, I., Clowsley, A. H., Lin, R., Lutz, T., Harrison, C., Green, E., Baddeley, D., Di Michele, L., & Soeller, C. (2018). True molecular scale visualization of variable clustering properties of Ryanodine receptors. *Cell Reports*, **22**(2), 557–567.

Kallestrup-Lamb, M., Marin, A. O. K., Menon, S., & Søgaard, J. (2024). Aging populations and expenditures on health. *The Journal of the Economics of Ageing*, **29**, 100518.

Kazakova, D., Colman, M. A., Pradhan, A., Gudaitis, L., Nys, L., Cools, B., Rega, F., Vandenberk, B., Terracciano, C., Roderick, H. L., Sipido, K. R., & Dries, E. (2025). Early onset of Ca^{2+} waves and synchronization in multicellular clusters facilitate focal arrhythmogenesis in human heart failure. *bioRxiv*. https://www.biorxiv.org/content/10.1101/2025.05.02.651991v1

Kolstad, T. R., van den Brink, J., MacQuaide, N., Lunde, P. K., Frisk, M., Aronsen, J. M., Norden, E. S., Cataliotti, A., Sjaastad, I., Sejersted, O. M., Edwards, A. G., Lines, G. T., & Louch, W. E. (2018). Ryanodine receptor dispersion disrupts Ca^{2+} release in failing cardiac myocytes. *eLife*, **7**, e39427.

Lim, W. S., Wong, S. F., Leong, I., Choo, P., & Pang, W. S. (2017). Forging a frailty-ready healthcare system to meet population ageing. *International Journal of Environmental Research and Public Health*, **14**(12), 1448.

Litwin, S. E., Zhang, D., & Bridge, J. H. B. (2000). Dyssynchronous Ca^{2+} sparks in myocytes from infarcted hearts. *Circulation Research*, **87**(11), 1040–1047.

Louch, W. E., Bito, V., Heinzel, F. R., Macianskiene, R., Vanhaecke, J., Flameng, W., Mubagwa, K., & Sipido, K. R. (2004). Reduced synchrony of Ca^{2+} release with loss of T-tubules-a comparison to Ca^{2+} release in human failing cardiomyocytes. *Cardiovascular Research*, **62**(1), 63–73.

Louch, W. E., Hake, J., Mørk, H. K., Hougen, K., Skrbic, B., Ursu, D., Tønnessen, T., Sjaastad, I., & Sejersted, O. M. (2013). Slow Ca^{2+} sparks de-synchronize Ca^{2+} release in failing cardiomyocytes: Evidence for altered configuration of Ca^{2+} release units? *Journal of Molecular and Cellular Cardiology*, **58**, 41–52.

Lu, L., Guo, J., Hua, Y., Huang, K., Magaye, R., Cornell, J., Kelly, D. J., Reid, C., Liew, D., Zhou, Y., Chen, A., Xiao, W., Fu, Q., & Wang, B. H. (2017). Cardiac fibrosis in the ageing heart: Contributors and mechanisms. *Clinical and Experimental Pharmacology & Physiology*, **44**, (Suppl 1), 55–63.

Meschiari, C. A., Ero, O. K., Pan, H., Finkel, T., & Lindsey, M. L. (2017). The impact of aging on cardiac extracellular matrix. *Geroscience*, **39**(1), 7–18.

Nakou, E. S., Parthenakis, F. I., Kallergis, E. M., Marketou, M. E., Nakos, K. S., & Vardas, P. E. (2016). Healthy aging and myocardium: A complicated process with various effects in cardiac structure and physiology. *International Journal of Cardiology*, **209**, 167–175.

Shah, C., Jiwani, S., Limbu, B., Weinberg, S., & Deo, M. (2019). Delayed afterdepolarization-induced triggered activity in cardiac purkinje cells mediated through cytosolic calcium diffusion waves. *Physiological Reports*, **7**(24), e14296.

Sheard, T. M. D., Hurley, M. E., Colyer, J., White, E., Norman, R., Pervolaraki, E., Narayanasamy, K. K., Hou, Y., Kirton, H. M., Yang, Z., Hunter, L., Shim, J., Clowsley, A. H., Smith, A. J., Baddeley, D., Soeller, C., Colman, M. A., & Jayasinghe, I. (2019). Three-dimensional and chemical mapping of intracellular signaling nanodomains in health and disease with enhanced expansion microscopy. *ACS Nano*, **13**(2), 2143–2157.

Sheard, T. M. D., Hurley, M. E., Smith, A. J., Colyer, J., White, E., & Jayasinghe, I. (2022). Three-dimensional visualization of the cardiac ryanodine receptor clusters and the molecular-scale fraying of dyads. *Philosophical Transactions of the Royal Society of London Series B: Biological Sciences*, **377**(1864), 20210316.

Sheard, T. M. D., & Jayasinghe, I. (2021). Enhanced expansion microscopy to measure nanoscale structural and biochemical remodeling in single cells. In P. Guichard, & V. Hamel (Eds.), *Methods in Cell Biology* (pp. 147–180). Academic Press.

Shen, X., van den Brink, J., Bergan-Dahl, A., Kolstad, T. R., Norden, E. S., Hou, Y., Laasmaa, M., Aguilar-Sanchez, Y., Quick, A. P., Espe, E. K., Sjaastad, I., Wehrens, X. H., Edwards, A. G., Soeller, C., & Louch, W. E. (2022). Prolonged β-adrenergic stimulation disperses ryanodine receptor clusters in cardiomyocytes and has implications for heart failure. *eLife*, **11**, e77725.

Soeller, C., Jayasinghe, I. D., Li, P., Holden, A. V., & Cannell, M. B. (2009). Three-dimensional high-resolution imaging of cardiac proteins to construct models of intracellular Ca^{2+} signalling in rat ventricular myocytes. *Experimental Physiology*, **94**(5), 496–508.

Song, L.-S., Sobie, E. A., McCulle, S., Lederer, W. J., Balke, C. W., & Cheng, H. (2006). Orphaned ryanodine receptors in the failing heart. *Proceedings of the National Academy of Sciences of the United States of America*, **103**(11), 4305–4310.

Steele, E. M., & Steele, D. S. (2014). Automated detection and analysis of Ca^{2+} sparks in x-y image stacks using a thresholding algorithm implemented within the open-source image analysis platform ImageJ. *Biophysical Journal*, **106**(4), 566–576.

Tian, D., & Meng, J. (2019). Exercise for prevention and relief of cardiovascular disease: Prognoses, mechanisms, and approaches. *Oxidative Medicine and Cellular Longevity*, **2019**, 3756750.

Tillberg, P. W., Chen, F., Piatkevich, K. D., Zhao, Y., Yu, C.-C., English, B. P., Gao, L., Martorell, A., Suk, H.-J., Yoshida, F., DeGennaro, E. M., Roossien, D. H., Gong, G., Seneviratne, U., Tannenbaum, S. R., Desimone, R., Cai, D., & Boyden, E. S. (2016). Protein-retention expansion microscopy of cells and tissues labeled using standard fluorescent proteins and antibodies. *Nature Biotechnology*, **34**(9), 987–992.

Waddell, H. M. M., Mereacre, V., Alvarado, F. J., & Munro, M. L. (2023). Clustering properties of the cardiac ryanodine receptor in health and heart failure. *Journal of Molecular and Cellular Cardiology*, **185**, 38–49.

Walker, M. A., Williams, G. S. B., Kohl, T., Lehnart, S. E., Jafri, M. S., Greenstein, J. L., Lederer, W. J., & Winslow, R. L. (2014). Superresolution modeling of calcium release in the heart. *Biophysical Journal*, **107**(12), 3018–3029.

Watkins, M., & Overton, L. (2025). The cost of caring: A scoping review of qualitative evidence on the financial wellbeing implications of unpaid care to older adults. *Ageing & Society*, **45**(7), 1465–1492.

Additional information

Data availability statement

The full RyR imaging dataset and the Python analysis package can be found at the Zenodo repository https://doi.org/10.5281/zenodo.18925439.

Competing interests

None declared.

Author contributions

Concept: M.A.C. Study design: M.A.C. and M.E.H. Wet-lab experiments: M.E.H. Data analysis: M.E.H., M.A.C., D.C. and A.P.B. Visualization: M.E.H., M.A.C. and D.C. Drafting: M.E.H., M.A.C. and A.P.B. Editing: all authors.

Funding

This work was supported by a Medical Research Council Career Development Award (MR/V010050/1) awarded to M.A.C. and supporting M.E.H. D.C. is supported by a Human Frontier Science Program grant (RGP010/2024) awarded to M.A.C.

Acknowledgements

The authors would like to thank Melanie Reay for her tireless dedication to the welfare of the ageing animals, Liam McCormick for contributing to the initial set-up and literature review, Derek Steele for his help with calcium imaging and analysis and the Leeds Bioimaging facility.

Generative AI statement

Generative AI was not used in the preparation of this article.

Keywords

ageing, calcium sparks, computational modelling, excitation–contraction coupling, rat model, RyR, super-resolution imaging

Supporting information

Additional supporting information can be found online in the Supporting Information section at the end of the HTML view of the article. Supporting information files available:

Peer Review History